A THERMAL INERTIA APPROACH TO PRECISION IRRIGATION USING UNMANNED AERIAL VEHICLES COUPLED WITH HIGH-RESOLUTION MULTISPECTRAL IMAGERY

by

KEVIN JAMES WIENHOLD

THESIS

Submitted in partial fulfillment of the requirements
for the degree of Master of Science in Civil Engineering at
The University of Texas at Arlington
December, 2017

Arlington, Texas

Supervising Committee:

Nick Z. Fang, Supervising Professor
Dong-Jun Seo
Yu Zhang
Xinbao Yu
Michael J. Shultz

ACKNOWLEDGEMENTS

I would like to thank and acknowledge each member of my graduate committee for their individual contributions towards my master's degree: Dr. Fang for continually encouraging me to think deeper, to focus on the practical, and for both *fully supporting* and *swiftly rejecting* my ideas, well- and ill-conceived, respectively (see *SELDOM*); Dr. Seo for providing difficult yet rewarding coursework and working me past my perceived potential; Dr. Zhang for advancing my knowledge in hydrology; Dr. Yu for generously providing me with whatever I asked; and Dr. Shultz for his excellent advice, counsel and friendship.

I would also like to thank my research colleagues, Daniel Li, Shang Gao, Cassie Zhang, Han Jiang and Trevor Stull. Each has helped with this research in a major way, whether assisting with field work, technical assistance with coding or simply covering my teaching assistant duties.

A hearty thanks to the City of Arlington and the staff at Meadowbrook Park Golf Course for participating in this study. Also a big thanks to the National Weather Service and River Forecast Center of Fort Worth for providing the meteorological data used in this research.

I would especially like to thank my grandmother, Doris Wienhold, who is my biggest supporter, my father, Robert Wienhold, for his continued encouragement and praise, my mother, Linda Randolph, for stimulating my interests in science and nature at an early age, and my fiancée, Wendy Earle, who has believed in me ever since I was taking night classes in community college, who has continued to love me through all of my processes.

November 28, 2017

ABSTRACT

A Thermal Inertia Approach to Precision Irrigation using Unmanned Aerial Vehicles Coupled with High-Resolution Multispectral Imagery

Kevin James Wienhold, M.Sc.
The University of Texas at Arlington, 2017

Supervising Professor: Nick Z. Fang

Soil moisture is a critical variable in the optimization of irrigation scheduling in water resources management. Despite using tens to hundreds of thousands of gallons of water each day, many golf courses rely on a sparse network of point measurements to estimate irrigation requirements for turfgrass management. This study describes a novel system known as *Precision Irrigation Soil Moisture Mapper* (PrISMM) in which an unmanned aerial vehicle equipped with multispectral sensors is used to estimate volumetric water content (VWC) at a golf course using a thermal inertia approach. *PrISMM* consists of three central components, including (1) high-resolution thermal and optical remotely-sensed data, (2) site-specific soil analysis, and (3) surface energy balance modeling. The objective is to evaluate the feasibility of spatially-variable irrigation management for a golf course in north central Texas using *PrISMM*. Multispectral data are collected during the fall of 2017 in the visible, near infrared and longwave infrared (thermal) spectrum using a UAV capable of rapid and safe deployment for daily time-series estimates. Each data set consists of two flights collected on the same day, including a morning and midday flight. Diurnal temperature variations were then related to ground heat flux to derive thermal inertia. Using thermal and physical soil properties, thermal inertia estimates are converted to daily VWC estimates with a resolution of 8.6 cm. The accuracy of *PrISMM* is quantified using ground truthing with a time domain

reflectometry soil moisture sensor. The model produces good estimates for VWC with an average coefficient of correlation of (r) = 0.89 and coefficient of determination of (R^2) = 0.79. Findings from this study indicate that *PrISMM* offers superior spatial and temporal resolution compared to *in situ* methods and may be implemented to precisely irrigate urban landscapes, thus saving millions of gallons of water annually.

TABLE OF CONTENTS

LIST OF FIGURES

LIST OF TABLES

Chapter 1

Introduction and Literature Review

In recent decades, increasing rates of urbanization and population growth have intensified pressure on managers of freshwater resources to satisfy demand for a diverse group of users. Today, half of the global population lives in urban cities which is projected to increase to two-thirds by the year 2050 (United Nations 2014). These pressures are magnified in arid and semi-arid regions where scarcity and high water demand prevail, such as north central Texas. Pressures on water supply will be further exacerbated in many regions from impacts of climate change, resulting in higher summer temperatures, prolonged periods of drought, and lower catchment water yields (Brookes et al. 2010; Ficklin et al. 2012; Liu et al. 2013). In order to cope with these issues and meet growing demand, many urban centers are moving away from traditional means of water supply and towards integrated water management systems, including large-scale water projects such as the Integrated Pipeline (IPL) project in Texas (Tijerina et al. 2016), water reuse and conservation methods, and managing water demand itself (Chung et al. 2009). The development or augmentation of water supply systems, however, requires long-term planning and significant monetary investments and may not be feasible in regions where freshwater is already over-allocated. Many governmental and regulatory agencies have therefore shifted emphasis towards water conservation and demand management which tends to be significantly cheaper and more responsive to the uncertainties of climate change (Boland 1997).

Water conservation and demand management are essential strategies in arid and semi-arid regions where irrigation dominates the usage of freshwater by rural and urban users alike. The Texas Water Development Board (TWDB) Water Use Survey reported in 2015 that irrigation by public and industrial water systems accounted for approximately 51 percent of water use in the state of Texas, totaling an estimated 5.22 million mega liters (ML) (4.23 million ac-ft) (2017). The largest

categorical user of water in Texas is irrigated agriculture followed by urban-municipal uses with landscape irrigation as its largest sub-user. Turfgrass is the central component of many urban-municipal landscapes, found in parks, athletic fields, residential, institutional, and commercial lawns and golf courses in particular. Cabrera et al. (2013) estimated that for 2010, golf courses occupied 465 sq. km throughout Texas with a total annual water usage of 0.449 ML (0.364 million ac-ft). When combined with golf courses, low-end estimates for landscapes constitute 46.6% of the total water use within the urban/municipal sector, accounting for 12.6% of the total annual demand for all activities in Texas during 2010 (Cabrera et al. 2013). Turfgrass has therefore been a major focus of urban water-use efficiency and irrigation studies for several decades (Fenstermaker-Shaulis et al. 1997; Trenholm et al. 2000; Wu and Bauer 2012).

The immense expenditure of freshwater on urban landscaping implies an opportunity for significant cost and water savings through more efficient irrigation delivery systems. Many approaches to improving efficiency have been proposed and implemented, ranging from potential evapotranspiration-based irrigation scheduling, water capture and reuse, "xeriscaping", or, landscaping which reduces the need for supplemental irrigation water, and *in situ* soil moisture sensors for time-based irrigation control (Bogena et al. 2007; St. Hilaire et al. 2008). This study also explores the use of soil moisture (SM) as a decision variable for irrigation management; however, instead of using *in situ* sensors, SM is remotely-sensed with the aid of an unmanned aerial vehicle (UAV). Although *in situ* sensors are a more direct measurement, estimates are fixed and limited in location and therefore cannot represent the spatial variability of SM. UAVs on the other hand can achieve excellent data density and continuity and may be operated in most *visual meteorological conditions* (VMC). A primary goal of this research is to replace point estimates with daily, continuous, surface soil moisture (SSM) estimates for an actual golf course with the objective of reducing over-watering and preventing under-watering through precision irrigation.

This study describes a novel system known as *Precision Irrigation Soil Moisture Mapper* (PrISMM) in which high-resolution, SSM estimates are derived from thermal inertia methods utilizing a UAV as a thermal and optical remote sensing platform. To the author's knowledge, novelty of this research exists in the following concepts not yet documented in the literature: (1) the application of a UAV for the detection of SSM for turfgrass management; (2) the application of UAVs for golf course irrigation management; and (3) the application of the thermal inertia method for the detection of soil moisture using UAV remotely-sensed data. The purpose of this research is to evaluate the feasibility of spatially-variable irrigation management for a golf course in north central Texas using *PrISMM*. If proven feasible, UAV-derived SSM maps will then drive a time-based irrigation system, delineated into irrigation management zones. Findings from this study indicate that *PrISMM* offers superior spatial and temporal resolution compared to *in situ* methods and may be implemented to precisely irrigate urban landscapes, thus saving hundreds-of-thousands of gallons of water annually.

This chapter is organized as follows: Section 1.1 presents the basic principles of irrigation requirements based on soil moisture content. Section 1.2 presents an overview of *in situ* sensor technology. Section 1.3 provides a history and overview of general remote sensing techniques for soil moisture estimation and a review of previous studies. Methods are collated and summarized into four groups, including (1) microwave remote sensing, (2) optical remote sensing, (3) temperature index remote sensing, and (4) thermal inertia remote sensing. This section also discusses the physical principles, advantages and disadvantages of these methods. Section 1.4 discusses the utilities and advantages of unmanned aerial vehicles in remote sensing along with a review of previous studies in the applications of hydrology and agricultural management.

1.1. Soil and Irrigation

Soil moisture (SM) is a critical variable in the optimization of irrigation scheduling in water resources management. In order to keep turfgrass healthy and playable for the game of golf, the volumetric water content (VWC) of the soil must be used to help determine irrigation requirements based with respect to several factors. Soil texture for instance determines important properties such as *permanent wilting point* (the minimum soil moisture content in which a plant can extract water), *field capacity* (the soil moisture content remaining after a saturated column of soil is drained by gravity) and *plant available water* (the difference between *field capacity* and *permanent wilting point*). The depth of the root zone determines the frequency of required irrigation –with deeper roots requiring less frequent irrigation. The evapotranspiration rate determines how much water will be lost from the soil through evaporation and transpiration and must be calculated from local meteorological data. The evapotranspiration rate will further be impacted by the length of grass, where frequent mowing can actually promote greater water use efficiency. The amount of organic matter in the soil can increase the *plant available water*, especially in sandy soils where porosity is high. Organic matter mixed into clay soils also breaks up soil colloids, allowing better percolation. The soil bulk density which can be increased by compaction and decreased by cultivation influences the infiltration rate of the soil, hence the amount of generated runoff. Thus, when soil becomes compacted, higher amounts of runoff and less percolation occurs. In contrast, cultivation reduces runoff by increasing percolation.

1.2. *In Situ* Sensing of Soil Moisture

Soil moisture (SM) is also highly variable in both time and space which often renders it a major source of uncertainty in the hydrologic sciences (Wang and Qu, 2009). Despite high-variability and uncertainty, many golf courses rely on a sparse network of point measurements to estimate the spatial distribution of water availability at the turfgrass root zone. The spatio-temporal variability of SM is in turn influenced by many factors including soil composition, vegetation cover,

climate, the depth of groundwater and topography. Unfortunately, the only means of directly measuring the VWC of soils is by using the gravimetric method to first determine *gravimetric water content* (GWC), or, the mass of water *per* mass of dry soil. It is measured by first weighing a soil sample, then oven-drying the sample to remove all water content, then re-weighing the dried mass. Despite its accuracy and simplicity, the gravimetric method is also time-consuming and destructive and therefore cannot account for the temporal variability of SM. All other methods for determining VWC are indirect measurements in which a secondary property is measured to infer VWC through calibration using GWC. Today, many *in situ* methods for estimating VWC exist and should be selected based on the objective of the measurement (Topp 2003).

Neutron thermalization probes were among the first instruments used for VWC field measurements. Here, a small radioactive material is stored in the instrument which releases high-energy epithermal neutrons into the soil. Some of the emitted neutrons interact with hydrogen atoms in which they are slowed down, referred to as *thermal neutrons*. The probe then detects the amount of thermalized neutrons which are directly related to the concentration of hydrogen atoms in water, and hence, VWC of the soil. The advantages of neutron probes include a large radius of influence (10 to 20 cm) which compensates for high spatial variability of SM and a decreased sensitivity to soil salinity and temperature. Due to the radioactive source, radiation certification is required which prohibits the device from being left unsupervised in the field, preventing the possibility of a continuous record of VWC. A relatively new system called *Cosmos* compares the number of incoming, naturally occurring epithermal neutrons from the atmosphere against the number reflected by the soil to estimate SM over a wide footprint (Shuttleworth et al. 2010); this system, however, is prohibitively expensive.

The Dual Needle Heat Pulse (DNHP) technique exploits the theory that the heat storing ability of soil is strongly related to VWC. One needle emits heat while the other needle measures

heat. The maximum temperature rise over a given time period is used to calculate heat capacity which through calibration can be converted to VWC. The placement of the needles in the soil is crucial however, and a deflection of as little as 1 mm can cause a 6 percent reduction in accuracy (Kluitenberg et al. 1995). Accuracy is also susceptible to temperature gradients in the soil. The sensitivity of needle deflection combined with a very small volume of influence renders this technique unusable for many soils and applications. The DNHP technique, however, is used in this study in a laboratory setting to determine soil physical parameters such as thermal conductivity and specific heat.

The time domain reflectometry (TDR) methods used in this study measure the travel time of an electromagnetic pulse traveling down a pair of stainless steel guide rods inserted into the soil, and then traveling back up the rods to a reference node. The speed of the wave in the soil is a function of the bulk dielectric permittivity (ε) of the soil matrix. When an electromagnetic field is formed between two oppositely charged electrodes, a dielectric material known as a capacitor will temporarily store the EM field. The dielectric constant is defined as the ability to store charge. Air has a dielectric permittivity (charge storing ability) of 1, organic matter between 1 – 5, soil minerals between 2 – 5, ice around 5 and water around 80. A dry soil containing only minerals, organic materials and air will have a dielectric permittivity between 2 – 3 while fully-saturated soils have a dielectric permittivity around 40. Since the composition of soils is relatively constant in the field, the only parameters that vary significantly with time are air and water content, thus allowing VWC to be inferred. The total dielectric of soil is composed of individual constituents with weighting fractions that add to unity:

$$\varepsilon_t^b = \varepsilon_m^b V_m + \varepsilon_a^b V_a + \varepsilon_w^b \theta + \varepsilon_{om}^b V_{om} + \varepsilon_i^b V_i \quad (1\text{-}1)$$

where ε is dielectric permittivity, b is a constant of approximately 0.5, and subscripts t, m, a, om, i and w represent total, mineral soil, air, organic matter, ice, and water. The equation can then be rearranged for water content:

$$\theta = \frac{1}{\varepsilon_w^{0.5}} \varepsilon_t^{0.5} - \frac{\varepsilon_m^{0.5} V_m + \varepsilon_a^{0.5} V_a + \varepsilon_{om}^{0.5} V_{om} + \varepsilon_i^{0.5} V_i}{\varepsilon_w^{0.5}} \quad (1\text{-}2)$$

Because the dielectric constant of water (ε = 80) is significantly greater than that of air (ε = 1) and soil solids (ε = 3 to 7), TDR sensors can exploit this relationship to consistently provide reasonably accurate measurements of VWC for many soils (Nadler, 1991; Jacobsen et al. 1993; Ponizovsky et al. 1999; Yu et al. 2015).

1.3. Remote Sensing of Soil Moisture

SM is a critical link between water and energy exchanges within the hydrosphere, atmosphere and biosphere (Zhang et al. 2014). Recognizing this importance, remote sensing of SM began in the 1950s in which point estimates were determined using empirical techniques combined with instruments such as colorimeters and spectrophotometers (Brook 1952; Kojima 1958). Spatiotemporal estimates for SM emerged with applications in satellite sensor technology offering global coverage. The first estimations of SM using satellite data began appearing in the literature in the mid-1970s with the advent of Landsat 1 (Pohn et al. 1974; Kahle 1976; Price, 1977). Remote sensing of SM estimation is typically divided into three categories: (1) microwave remote sensing, including active and passive; (2) optical and thermal remote sensing; and (3) synergistic methods using combined methods of microwave, optical and/or thermal technology. The next three sub-sections will focus on several of these methods, including microwave methods, optical methods, temperature index methods and thermal inertia methods.

1.3.1. Microwave Methods

In the 1970s, the launch of the Nimbus 5 made possible the estimation of SM from a microwave spectrometer (Schmugge 1977). Passive and active satellite microwave sensors have since become the most commonly used technologies for SM estimation (Coppo et al. 1990; Jackson 1993; Li et al. 2002). Both passive and active sensors relate backscatter coefficients determined by the dielectric constants of water and soil particles to SM using empirical models (Zribi et al. 2013; Baghdadi et al. 2011) and physical models (Santi et al. 2013; Cho et al. 2015a; Jonard et al. 2015). Observation satellites such as the European Space Agency's *Soil Moisture and Ocean Salinity* (SMOS) and the *Advanced Scatterometer* (ASCAT) provide a time-series of SM estimates with global coverage. NASA's *Soil Moisture Active Passive* (SMAP) utilizes an L-band radiometer (V, H, and 3rd and 4th Stokes parameter polarizations) and the now defunct L-band radar (VV, HH, and HV polarizations) which estimates global water flux at the earth's surface (top 5-cm) (NASA 2017a). The primary limitation of these satellite observations is the spatial resolution, which is usually measured on the order of square kilometers. Several other satellites offer very-high spatial resolutions (1-5 m), including DEIMOS, DMC, PLEIADES and WorldView2, but lack frequent observations.

1.3.2. Optical Methods

The relationship between SM and soil spectral reflectance was first documented in the experimental work of Ångström (1925). Extensive laboratory experiments have since been conducted, inferring soil moisture content (SMC) from spectral measurements for many different soil types. These laboratory studies reveal that as SMC increases, reflectance values in the solar domain (0.4 – 2.5 μm) decrease, leading to a darkening effect (Jackson et al. 1976; Dalal 1986). Bowers et al. used spectrophotometry to estimate SM for three different textured soils, noting a linear relation between the absorbance at 1.9 μm and SMC (1972). Bach et al. observed the spectral response of soils with varying degrees of SMC and determined that the darkening effect was a

function of the reflectance of dry soil particles and the refractive index of water (1994). Lobell et al. developed an exponential model to describe the relationship of soil reflectance and SMC, noting that the shortwave-infrared (SWIR) region was the most responsive, thus offering greater SMC predictive skill than the visible (VIS) and near-infrared (NIR) regions (2002). Liu et al. examined eighteen soils during the drying process with a spectroradiometer, noting non-linearities associated with absorption amplitude of wavelengths with the strongest SMC correlation in the 1.622 μm waveband (2010).

Optical remote sensing techniques are now widely applied to airborne and satellite data, estimating SMC for a wide range of conditions (Muller and Décamps 2001; Zeng et al. 2004). These methods can be divided into two categories but are typically used in concert: (1) the spectral reflectance method, and (2) the vegetation index method. The spectral reflectance method measures absorption amplitude of wavelengths located in water absorption bands to develop empirical and semi-empirical relationships with SMC (Fabre et al. 2015). Selected portions of the electromagnetic spectrum are plotted against the reflectance values of an object to reveal unique spectral signatures. Li et al. for example utilized Landsat-7 *Enhanced Thematic Mapper Plus* (ETM+) and Landsat-8 *Operational Land Imager* (OLI) to extract volumetric surface SMC at the field scale (30 m) for rice paddies using VIS, NIR and SWIR bands with a correlation coefficient of 0.78 (2016).

One challenge with these techniques is the tendency for atmospheric conditions to reduce and degrade (sometimes drastically) soil reflectance signatures. To overcome this deficiency, optical remote sensing methods are usually combined with vegetation indices and thermal methods. Here, aerial and satellite imagery using radiometrically-calibrated sensors capture electromagnetic radiation in the visible, i.e., red, green and blue bands (VIS), near infrared (NIR), shortwave infrared (SWIR), and thermal infrared (TIR) ranges. Electromagnetic energy is then decomposed into discrete bands and recombined to display different features of land and water surfaces. Vegetation

indices, such as the *normalized difference vegetation index* (NDVI) and the *vegetation condition index* (VCI) are used to enhance SM estimates by detecting water stress in green plants. Vegetation indices operate on the principle that live green plants are evolved to strongly absorb solar radiation in the visible spectrum while the cell structure of their leaves strongly reflect the solar radiation not used in photosynthesis, i.e., NIR. The equation for NDVI for example is given as the difference of reflectance values between the NIR and red bands, divided by the summation of NIR and red:

$$NDVI = \frac{NIR - red}{NIR + red} \tag{1-3}$$

where reflectance is usually represented by a digital number (DN) between 0 – 255. A high NDVI value for example is associated with healthy vegetation which in turn indicates low water stress (NASA 2017b). VCI accounts for short-term water-related NDVI fluctuations from long-term ecosystem changes by considering multi-year NDVI values (Kogan, 1995):

$$VCI = \frac{NDVI - NDVI_{min}}{NDVI_{max} - NDVI_{min}} \tag{1-4}$$

where $NDVI_{min}$ and $NDVI_{max}$ are the seasonal minimum and maximum NDVI values, respectively. NDVI, VCI and other similar indices can be directly related to vegetation growth and drought conditions which is then used to indirectly estimate SMC.

The main shortcoming with vegetation index methods is the temporal delay between SM deficiency or abnormal reduction in rainfall and the response of the vegetation, leading some researchers to refer to vegetation indices as after-effects (Qin et al. 2008). Thus, NDVI is more appropriate for monitoring trends and long-term drought as opposed to frequent time-series estimates for SMC. Vegetation indices are also sensitive to cloud cover and solar zenith and azimuth angles which depend on vegetation canopy architecture and leaf angle distribution (Kimes et al. 1985; Sellers 1985), requiring extensive radiometric calibration and ground truthing. Despite these

shortcomings, there remains a growing interest in developing these capabilities. While reflected visible and near infrared radiation interacts with only the topmost layer, the wide availability of multi- and hyperspectral-equipped satellites render this method more operational than microwave. Another advantage of optical remote sensing is the ease of use: the *United States Geological Survey* (USGS) and *National Aeronautical Space Administration* (NASA) offer VIS, NIR, SWIR and TIR data free-of-charge with global coverage and fine spatial resolutions. Indeed, future satellite launches are planned which will increase the availability and frequency of hyperspectral products with missions such as the Italian Space Agency's *PRecursore IperSpettrale della Missione Applicativa* (PRISMA) and the Space Agency of the German Aerospace Center's *Environmental Mapping and Analysis Program* (EnMAP).

1.3.3. Temperature Index Methods

Thermal remote sensing provides a unique advantage over optical techniques in that longwave radiation reflected as heat is comprised of thermal energy extending several layers below the surface to varying depths. For instance, near surface layers can experience alternate heating and cooling to depths of 50 to 100 cm during a single day while the mean seasonal temperature of bedrock may extend to depths of 10 m or more (Sabins 1997). Temperature inequities arise naturally in accordance with the physical properties of soil stratum through the mechanisms of solar radiation and heat transfer. SM partitions solar radiation into latent and sensible heat at the earth's surface (Vereecken et al. 2014) and can therefore linked to land surface temperature (LST) through surface energy balance modeling. Under the assumption of energy balance, LST is defined as the temperature of the earth's surface (for bare soils) or the temperature of the vegetation canopy (for densely-vegetated regions). Significant differences in thermal properties of water and soil make it possible to infer accurate SM estimates when soil composition, vegetation type and temporal meteorological conditions are known.

Thermal remote sensing methods are usually divided into two categories: (1) the temperature index method, and (2) the thermal inertia method (Zhang and Zhou, 2016). Thermal index methods relate LST to SMC through empirical equations. Here, temperature is related to the moisture content of soils, revealing areas of relative coolness when water evaporates (2007). As vegetation undergoes water stress, evapotranspiration decreases, followed by a measurable rise in the temperature of the vegetation canopy. Alternatively, when SMC is abundant, evapotranspiration increases and there is subsequent and measurable decrease in the vegetation canopy. Kogan introduced the concept of the *temperature condition index* (TCI) to estimate vegetation stress caused by temperature and excessive wetness (1995). Similar to VCI, multi-year, seasonal minimum and maximum temperature values are used to monitor drought conditions:

$$TCI = \frac{T_{max} - T}{T_{max} - T_{min}} \tag{1-5}$$

where T_{min} and T_{max} are minimum and maximum observed temperatures, respectively. Here, a high TCI value in the middle of a season should indicate unfavorable conditions most akin to drought. When TCI is used as the sole indicator of SM, however, the predictive skill is typically poor. In order to improve TCI-derived drought assessments by accounting for precipitation, Kogan combined VCI and TCI by introducing weighting factors:

$$V/TCI = 0.70\,VCI + 0.30\,TCI \tag{1-6}$$

where weighting factors are determined experimentally. Kogan reported that V/TCI was a better indicator for drought assessment than either TCI or VCI used separately. Similar methods combined with machine learning have been used elsewhere to estimate VWC with good results (Hassan-Esfahani *et al*, 2015).

Idso et al. developed the *crop water stress index* (CWSI) based on canopy-air temperature differences and air vapor pressure deficits for quantifying water stress (1981):

$$CWSI = \frac{(T_c - T_a) - (T_c - T_a)_{min}}{(T_c - T_a)_{max} - (T_c - T_a)_{min}} \quad (1\text{-}7)$$

where $(T_c - T_a)$ is the difference between the vegetation canopy temperature and air temperature, $(T_c - T_a)_{max}$ is the canopy-vegetation difference for the maximum daily crop water stress before irrigation, i.e., the lower boundary condition for potential transpiration, and $(T_c - T_a)_{min}$ is the upper boundary condition for *no plant transpiration* conditions. Alderfasi et al. developed a baseline equation to calculate CWSI for water stress monitoring and irrigation scheduling of wheat with promising results (2000). The *normalized difference temperature index* (NDTI) was developed by McVicar et al. which calculates potential water availability by taking the ratio of actual evapotranspiration (ET_a) to potential evapotranspiration (ET_p) (2007). The index utilizes a dual surface energy balance model in which vegetation and soil are treated as independent sources of heat flux. Extreme LSTs are obtained from aerodynamic impedance models and are treated as boundary conditions to remove the effect of seasonal variability of SM. Extensive forcing data such as leaf area index (LAI), humidity, vapor pressure, wind speed and solar radiation, however, render this method problematic when meteorological ground observations are spatially sparse.

1.3.4. Thermal Inertia Methods

Thermal inertia is an important property which represents a material's ability to resist changes to ambient temperature variation. Carslaw and Jaeger formulated the definition of thermal inertial by solving the heat flow equation for a material subject to periodic heating (1959):

$$P = \sqrt{\lambda \rho_b C} \quad (1\text{-}8)$$

where P (J m^{-2} K^{-1} s$^{-1/2}$) is the thermal inertia, λ (W m^{-1} K^{-1}) is the thermal conductivity, ρ_b (kg m^{-3}) is the bulk density and C (J kg^{-1} K^{-1}) is the specific heat capacity. As it relates to soils, soil thermal inertia (STI) is a measure of the daytime rise in temperature of the surface layer in which water content is implicit in each term (λ, ρ_b, C). In general, the presence of moisture in porous media such as soils increases STI due to the higher specific heat of water (Verstraeten et al. 2006). The principles of thermal inertia are applied to remote sensing by developing a relationship between diurnal temperature variations of land surfaces and ground heat flux [Eq. 2-6]. Corresponding changes in the earth's surface temperature can be modeled using the conservation of energy:

$$R_n = H + LE + G \tag{1-9}$$

where R_n (W m^{-2}) is net radiation resulting from incoming solar radiation, atmospheric radiation and earth emitted radiation, H is sensible heat flux, LE is the latent heat flux and G is ground heat flux. Here, land surface temperature (LST) is recorded twice daily, typically day/night, sunrise/sunset or a similar variant while ground heat flux is estimated from physical or empirical relationships with net radiation (Eq. 2-7). When the thermal and physical properties of near surface soils are known, thermal inertia can be used to infer the spatial variability of SM.

Thermal inertia studies using satellite remotely-sensed imagery begin appearing in the literature in the 1970s with the launch of Landsat 1 (Watson 1971; Pohn *et al.* 1974; Kahle 1976; Price 1977). The theory of thermal inertia finds its origins with the work of Jaeger who recognized that remotely-sensed TIR imagery can be used to quantitatively estimate the heat storing capacity of the moon's surface (1953). Jaeger solved the one-dimensional thermal diffusion equation of a uniform half-space (a region bounded by a plane on its upper side and extending downward to infinity) with constant thermal properties (1953):

$$D\frac{\partial^2 T(z,t)}{\partial z^2} = \frac{\partial T(z,t)}{\partial t} \tag{1-10}$$

where T is the temperature at depth z (m) below the surface at time t (s) relative to solar noon and D ($\lambda\ \rho_b^{-1}\ C^{-1}$) is the thermal diffusivity of the half-space. Watson solved the diffusion equation by imposing surface boundary conditions as the energy balance between incoming solar and sky radiation, outgoing ground radiation, and conduction into the ground (1975):

$$-k\frac{\partial T\ (z,t)}{\partial z}|_{z=0} = -\varepsilon_s \sigma T^4 + I \tag{1-11}$$

where ε_s is the surface emissivity, $\sigma (5.67 \times 10^{-8}\ \mathrm{W{\cdot}m^{-2}{\cdot}K^{-4}})$ is the Stefan-Boltzmann constant and I is absorbed incoming radiation.

By the late 1970s and early 1980s, the importance of SM was widely recognized as one of several governing parameters in surface energy balance modeling in thermal inertia studies (Carlson et al. 1981; Carlson, 1986; Watson, 1982). Kahle (1977) and Watson (1982) proposed physical analytical solutions to the estimation of STI with one-dimensional periodic heat conduction equations. Kahle attempted to modify these methods for larger regions, noting uncertainties arising from the difficulty of estimating soil physical parameters at the regional scale (1977). Price assumed a linear relationship between latent and sensible heat and LST and calculated *STI* from absorbed solar energy by including terms for atmospheric transmissivity (τ_{sw}) and surface albedo (α) (1977):

$$STI = \frac{2\ \varphi\ \tau_{sw}(1-\alpha)\ C_1 \cos(\omega t - \vartheta_1)}{\omega^{1/2}\left[1+\alpha^2+\alpha\sqrt{2}\right]^{1/2}\left[T_{day} - T_{night}\right]} \tag{1-12}$$

where φ (rad) is the solar constant, ϑ_1 (rad) is solar declination, ω (rad s^{-1}) is the frequency of diurnal variation and C_1 is the first term of a Fourier series analysis on surface temperature (T). Here, STI is estimated from thermal satellite measurements and atmospheric forcing data to infer otherwise unknown surface characteristics, thus eliminating the need for extensive ground auxiliary data. The

model is complicated, however, by uncertainties in the earth's atmosphere, including energy re-radiated into the atmosphere by moisture, reduction of transmittance by aerosols and molecular constituents, and nonlinearities in the resistance factor relating surface temperate and humidity to sensible and latent heat flux (Price, 1977). Idso et al. proposed a simple thermal inertia method using ground heat flux determined with empirical equations and twice the amplitude of LST variation. The major disadvantage of the model is that it requires the daily minimum and maximum LSTs from TIR imagery, hence, limiting the operability of the model due to infrequent satellite overpasses (1976). Xue and Cracknell (1995) approached the problem of TIR satellite imagery acquired during overpass times not coincident with the minimum and maximum LSTs by proposing correction factors in accordance with the sinusoidal behavior of daily surface temperature variation (1995). Maltese *et al.* demonstrated that these cosine correction factors are unnecessary when diurnal temperature variation is measured in reference to solar noon (2013).

Price proposed the dimensionless *apparent thermal inertia* (ATI) index which is the ratio of shortwave radiation absorption to the diurnal temperature variation:

$$ATI = 1000\pi \times \frac{(1-\alpha)\, C_1}{T(1{:}30\ p.m.) - T(2{:}30\ a.m.)} \tag{1-13}$$

where *1000π* is a scaling factor used to force the data to fall between the range of 0 – 255 to match other 8-bit satellite products. The primary advantage of ATI is that it can be derived solely from remote sensing data, thus eliminating the need for ground based observations. Due to its ease-of-use and broad operability, ATI has been used extensively in many remote sensing studies over widely varying regions. Yang et al. quantitatively estimated SMC applying ATI over ten experimental plots with different vegetation covers and soil water contents, finding good agreement for soils containing vegetation cover with an NDVI value of 0.35 or less (2012). Verstraeten et al. estimated SMC from METEOSAT imagery using ATI and a simple two-layer water balance

equation and validated using TDR measurements (2006). Veroustraete et al. performed SM estimation for soil profiles of 1 m for the province of Xinjiang using ATI combined with soil type classifications and MODIS data (2011). They concluded that ATI is suitable for the estimation of SMC in arid to semi-arid regions. Indeed, ATI shows promise for bare or lightly vegetated soils but the simplifying assumptions regarding surface energy balance and soil physical parameters adds to model uncertainty warranting additional caution with its use.

New generations of lightweight sensors have enabled the collection of high resolution, multi- and hyper-spectral imagery using small aircraft with applications in SM detection using thermal inertia methods. Minacapilli et al. derived thermal inertia estimates with a resolution of 4 m using an 11-band passive remote sensor attached to a low flying airplane. Here, the spatial distribution of P is used to estimate VWC by inverting Eq. 2-6 with good results. Maltese *et al.* used identical sensors as Minacapilli et al., achieving a standard error of ~0.01 using a three temperature approach phase correction to thermal inertia (3 m resolution) for the upper soil layer (2013). The authors further demonstrated that SMC can be linearly related to ground heat flux and surface temperature for lightly vegetated surfaces. Soliman et al. used an airborne thermal camera to study relationships between SM, mechanical resistance and thermal inertia (0.6 m resolution) for a vineyard with grass-covered soil and a standing grape canopy (2013). They found that despite the complex heating and cooling patterns of the vineyard, significant correlations exist between SM, mechanical resistance and thermal inertia.

In this paper, a thermal inertia approach is taken. By utilizing UAVs as a thermal and optical remote sensing platform, many of challenges associated with thermal and optical remote sensing (e.g., low spatial and temporal resolution) can be avoided (see Section 1.3).

Table 1-1 Comparison of remote sensing methods for estimation of soil moisture.

Category	Method	Advantages	Disadvantages	Example Studies
Microwave	Passive	High temporal resolutions, accurate SMC estimates over bare soil, not limited by cloud cover or time of day.	Low spatial resolutions, SMC estimates impaired by vegetation and surface roughness.	Choudhury et al. (1979), Ulaby et al. (1986), Schmugge & Jackson (1997).
	Active	Medium spatial resolutions, not limited by cloud cover or time of day.	Low temporal resolutions, SMC estimates impaired by vegetation and surface roughness.	Pierdicca et al. (2012), Al-Yari et al. (2014), Vereecken et al. (2014), Cho et al. (2015b).
Optical	Reflectance-based	High spatial resolutions, wide availability of satellites, hyperspectral technology promising, easily adapted to UAVs.	No surface penetration; Poor SMC correlation with dense vegetation, unable to penetrate cloud cover, not applicable at night.	Muller and Décamps (2001), Zeng et al. (2004), Fabre et al. (2015), Li et al. (2016).
	Vegetation Index	High spatial resolutions, wide availability of satellites, hyperspectral technology promising, easily adapted to UAVs for on-demand data collection.	Time lag between water stress and vegetation response, unable to penetrate cloud cover, not applicable at night.	Muller and Décamps (2001), Zeng et al. (2004), Fabre et al. (2015).
Thermal	Temperature Index	High spatial resolutions, wide availability of satellites, easily adapted to UAVs for on-demand data collection.	Poor SMC correlation with dense vegetation, unable to penetrate cloud cover, empirically-based.	Idso et al. (1981), Kogan (1995), Alderfasi et al. (2000), McVicar et al. (2007).
	Thermal Inertia	High spatial resolutions, wide availability of satellites, clear physical meaning, easily adapted to UAVs for on-demand data collection.	Poor SMC correlation with dense vegetation, unable to penetrate cloud cover, sensitive to atmospheric conditions.	Pohn *et al.* (1974), Kahle (1976), Price (1977), Carlson *et al.* (1981), Watson, (1982), Minacapilli *et al.* 2009, Maltese *et al.* (2013).

1.4. Unmanned Aerial Vehicles

Only fifteen years after the Wright brother's historic flight in 1903, the first UAV was invented: the *Kettering Bug* flying bomb (Valavanis and Kontitsis 2007). Today, UAVs serve as research, reconnaissance, and surveying platforms, often outperforming their manned aircraft counterparts in terms of efficiency, affordability and operational flexibility. In the last decade, UAVs have made possible the acquisition of very-high resolution remote sensing data that would

otherwise be cost-prohibitive and time-consuming if using traditional methods. Such platforms have consistently proven to match the standards of direct measurements while offering greater density and continuity of data (Turner et al. 2012). Technical advances leading to cost and size reductions in equipment such as of *global positioning systems* (GPS), *inertial measurement units* (IMU), *inertial navigation systems* (INS) and *real time kinematics* (RTK), provide not only centimeter-level positioning and accuracy but advanced auto-piloting, pre-defined flight routes and waypoint navigation (Agüera-Vega 2017).

UAVs coupled with improvements in structure from motion (SfM) photogrammetry, multispectral sensors and Light Detection and Ranging (LiDAR) technology have found recent and widespread applications in modern days. With the release of the Federal Aviation Administration's (FAA) Small Unmanned Aircraft Regulations released under Part 107 of the Federal Aviation Regulations in August of 2017, the usage of UAVs for civil and commercial use has continued to grow exponentially. According to a recent study, the integration of UAVs into the national airspace is estimated to add $82 billion to the US economy between 2015 and 2025 with 100,000 new jobs created by 2025. UAVs are currently being used in many industries such as wildfire mapping, agricultural monitoring, disaster management, law enforcement, weather monitoring, environmental monitoring and oil and gas exploration (Jenkins and Vasigh 2013). Current applications in civil engineering include the quantification of channel bathymetry using through-water photogrammetry (Shintani and Fonstad 2017), the detection of inundated areas in urban landscapes (Feng 2015), traffic monitoring and management (Kanistras et al. 2014), and channel morphology and hydrodynamic modeling (Tamminga 2014).

UAVs equipped with multispectral sensors represent an emerging technology capable of detecting and estimating SSM for irrigation and crop management (Hassan-Esfahani et al. 2015). Most remotely-sensed SM products are derived from satellite imagery and consist of a resolution

too course for precision irrigation, i.e., on the order of square kilometers. Alternatively, UAVs offer significant improvements for remote sensing at smaller scales (~ 1 km^2) including sub-decimeter resolution. By acquiring visible and near infrared (VIS-NIR) and thermal infrared (TIR) imagery with high resolution sensors from low altitudes, radiometric distortions arising from atmospheric effects are often negligible. This is especially important in regions dominated by cloud cover, which optical and thermal observations from satellites fail to penetrate. Furthermore, the relative ease and low cost of deploying UAVs for data acquisition ensures ideal overpass times.

Many UAV studies for agricultural management and monitoring vegetation status and health appear in the literature starting in the 2000s. Applications include measuring shrub biomass (Quilter and Anderson 2001), monitoring rangeland conditions (Hardin and Jackson 2005), classifying rangeland vegetation (Laliberte and Rango 2011), and vineyard management (Primicerio et al. 2012). Agricultural studies utilize vegetation indices from multispectral imagery, including applications in crop management and stress detection (Berni et al. 2009), estimating yield and crop biomass (Swain et al. 2010), and monitoring nitrogen status from fertilization experiments (Hunt 2005). Different crop types examined using UAV data include corn (Hunt 2005), wheat (Hunt et al. 2010), rice (Swain et al. 2007), and turfgrass (Xiang and Tian 2011; Zhang and Kovacs 2012).

To date, very few studies using UAVs for the estimation of SM have been conducted. Hassan-Esfahani et al. estimated spatial root zone SMC in an agricultural field using artificial neural networks combined with VIS-NIR and TIR high-resolution imagery. Data mining was applied to several indices, including NDVI, VCI, *enhanced vegetation index* (EVI), *vegetation health index* (VHI) and TCI, with good model predictive skill (R^2 = 0.94) (2015; 2017). Gonzalez-Dugo et al. determined the spatial variability of water status and irrigation needs for a pistachio farm using CWSI based on tree canopy temperature (2014). Hoffman et al. used thermal UAV data to determine the spatial variability of heat flux over a barley field and estimate evaporation using a two-source

energy balance modeling scheme (2016). To the author's best knowledge, a thermal inertia approach for the estimation of SM has never been attempted with UAVs. The author is thus motivated to develop a novel approach for the estimation of high-resolution, contiguous volumetric water content (VWC) using remote sensing techniques to be validated with *in situ* measurements. The UAV platform used in this study, *MavAir One*, is a powerful remote sensing octocopter equipped with thermal and optical sensors. *MavAir One* is shown over the study area, Meadowbrook Park Golf Course, during one of its missions in Figure 1-1.

Figure 1-1 *MavAir One* over Meadowbrook Park Golf Course, Arlington, TX.

Chapter 2

Approach/Methodology

The author hypothesizes that a multispectral remote sensing platform mounted to an unmanned aerial vehicle (UAV) can be used to capture daily aerial imagery for a given soil type and vegetation cover to estimate SSM. The presence or absence of SSM will produce unique spectral signatures which can be related to the VWC. When combined with vegetation indices, such as NDVI, and a knowledge of soil physical properties (soil type, bulk density, texture, thermal conductivity, etc.), a thermal inertia approach may be used. The predictive skill of the model can be validated with *in situ* measurements of VWC within the study area. If the method proves feasible, the UAV-derived VWC estimates may be used for spatially-distributed irrigation management. In order to develop this approach, several objectives are satisfied: (1) to select a study area for data collection, monitoring, and validation; (2) to obtain daily, high-resolution, multispectral imagery of the study area; (3) to collect daily field measurements of VWC for model validation; (4) to develop a novel computer script to solve for VWC using multispectral imagery, local meteorology and measured physical parameters; (5) to quantify the accuracy of the model using a linear least squares approach.

2.1. Methodology

The *Precision Irrigation Soil Moisture Mapper* (PrISMM) model consists of three central components, including (1) site-specific soil analysis, (2) high-resolution thermal and optical remotely-sensed data, and (3) surface energy balance modeling. In this study, diurnal temperature variations are related to ground heat flux to derive thermal inertia which is then used to solve for volumetric water content (VWC). Thermal inertia can be defined as (Carslaw and Jaeger 1959):

$$P = \sqrt{\lambda \rho_b C} \tag{2-1}$$

where P (J m^{-2} K^{-1} s$^{-1/2}$) is the thermal inertia, λ (W m^{-1} K^{-1}) is the soil thermal conductivity, ρ_b (kg m^{-3}) is the actual soil bulk density (including water) and C (J kg^{-1} K^{-1}) is the soil heat capacity that is expressed as (van Wijk and de Vries 1963):

$$\rho_b C = \rho_{bd} C_s + \theta \rho_w C_w \tag{2-2}$$

where ρ_{bd} (kg m^{-3}) is the dry bulk density of soil, ρ_w (~ 998 kg m^{-3}) is the density of water at room temperature, C_s (J kg^{-1} K^{-1}) and C_w (4,184 J kg^{-1} K^{-1}) are the heat capacities of the solid and liquid phases, respectively. Though C and λ are influenced by many factors, including dry bulk density, mineral composition, porosity and temperature, these factors remain relatively constant in the field. On the other hand, θ which is strongly related to C and λ can vary considerably. For this reason, much effort has been invested to formulate $C(\theta)$ and $\lambda(\theta)$ relationships with physical models (van Wijk and de Vries 1963; Johansen 1975; Lu et al. 2007) as well as empirical models (Kersten 1949).

Johansen (1975) provided accurate predictions of λ for a wide range of soils by introducing the concept of a normalized thermal conductivity, referred to as the *Kersten* number (K_e). The empirical model is given by:

$$\lambda = K_e\left(\lambda_{sat} - \lambda_{dry}\right) + \lambda_{dry} \tag{2-3}$$

where λ_{sat} and λ_{dry} (W m^{-1} K^{-1}) are the thermal conductivities of saturated and air-dry soils, respectively. The Kersten number is an empirical parameter which is a function of relative water content, S_r. Lu et al. (2007) found excellent agreement between measured and estimated λ values using the following expression for K_e:

$$K_e = \exp\left[\gamma\left(1 - S_r^{\gamma - \delta}\right)\right] \tag{2-4}$$

where $\delta = 1.33$ is a shape parameter and S_r is the ratio between the actual soil water content, θ (m^3 m^{-3}), and the saturated soil water content, θ_s (m^3 m^{-3}). The soil-texture dependent parameter, $\gamma = 0.96$ (-), is determined by the sand fraction (f_s) as given by Lu et al. (2007):

$$\gamma = 0.96 \quad (f_s > 0.40)$$
$$\gamma = 0.27 \quad (f_s \leq 0.40) \tag{2-5}$$

Idso et al. (1976) and Menenti (1984) proposed similar remote sensing methods to derive thermal inertia estimates from surface heat flux and surface temperature variation using the following relationship:

$$P_{rs} = \frac{2\Delta G}{\Delta T\sqrt{\omega}} \tag{2-6}$$

where ΔT (K) is the difference between the minimum and maximum daily surface temperature, ω (rad s^{-1}) is the angular velocity of the earth's rotation assuming a 24 h period (i.e., 2π/86,400 s) and ΔG (W m^{-2}) is the amplitude of the sinusoidally-varying ground heat flux during this period. Because the initial G is approximately 0 W m^{-2} at the early morning and hence negligible, ΔG is calculated as the magnitude of G at midday. G is typically estimated as a fraction of net radiation and some function of vegetation indices such as *NDVI* or leaf area index (LAI), albedo and/or surface temperature. There are many empirical equations available for estimating G for vegetated surfaces and are largely selected based on user experience. Several equations were tried in this study (Bastiaanssen 2000; Allen et al. 2007; Cuenca et al. 2013; Singh et al. 2008) with the best results obtained from Santanello and Friedl, based on diurnal patterns from SHAW simulations (2003):

$$\frac{G}{R_n} = A\cos\left(2\pi\frac{t + 10{,}800}{B}\right) \tag{2-7}$$

where t (s) is the time of data capture relative to solar noon. A (-) represents the maximum value of G/Rn while B (s) is used to adjust the diurnal phase amplitude of G/Rn, defined respectively as (Hoffman *et al*, 2016):

$$A = 0.0074\,\Delta T_s + 0.088 \tag{2-8}$$

$$B = 1729\,\Delta T_s + 65{,}013 \tag{2-9}$$

For simplicity, the calculation of net radiation was based on the methods used by Minacapilli et al. which proved to yield good results (2009). The full equation for R_n is defined as the sum of both incoming and outgoing short- (solar) and long- (thermal) wave radiation at the surface assuming steady state conditions (Melesse 2004):

$$R_n = R_{S\downarrow} - \propto R_{S\downarrow} + R_{L\downarrow} - R_{L\uparrow} - (1 - \varepsilon_s)R_{L\downarrow} \tag{2-10}$$

where $R_{S\downarrow}$ (W m^{-2}) is incoming shortwave radiation, $\propto$ is the combined soil and vegetation albedo, ε_s is the surface emissivity, $R_{L\downarrow}$ (W m^{-2}) is absorbed incoming longwave radiation and $R_{L\uparrow}$ is outgoing longwave radiation. Here, the soil/vegetation albedo is defined as the fraction of incident solar energy reflected by the surface which in turn is a function of the fraction of turfgrass and soil surface wetness. An approximate value for albedo is calculated for each as follows (Liang, 2004):

$$\alpha \simeq \sum_{i=1}^{n} w_i r_i \qquad i = 1, 2, \ldots, n \tag{2-11}$$

where r_i is the surface spectral reflectance for narrow bands and w_i are the weighting factors determined from the following equation (Menenti, 1984):

$$w_i = \frac{E_i^0}{\sum_{i=1}^{n} E_i^0} \qquad i = 1, 2, \ldots, n \tag{2-12}$$

where E_i^0 is the extraterrestrial solar irradiance for each narrow band, determined at the time of flight using a down-welling light sensor installed on the UAV. While not representative of the entire shortwave spectrum, the calculated albedo values for the turfgrass appeared to be reasonable (0.26 – 0.28), showing good agreement with grass albedo values (0.24 – 0.26) reported by Campbell and Norman (1998).

In the absence of solar radiation flux density measuring devices such as net radiometers and pyranometers, it has been suggested that under clear sky conditions, solar and sky radiances can be satisfactorily approximated using equations based on solar azimuth, zenith and astronomical distance (Watson, 1982). We assume that the incoming radiation is uniform over the entire golf course. The calculation for $R_{S\downarrow}$ assuming clear sky conditions becomes (Xu 2014):

$$R_{S\downarrow} = \frac{G_{sc} \cos\varphi \, \tau_{sw}}{d^2} \tag{2-13}$$

where G_{sc} (1,367 W/m^2) is the solar constant, φ (rad) is the angle of solar incidence, d (AU) is the relative earth-sun distance in astronomical units which varies between 0.9833 AU (3–5 January) and 1.0167 AU (3–7 July) (Sun et al. 2013). An approximate expression is used to calculate d based on the Julian day of the year (Achard and D'Souza 1994):

$$\frac{d}{AU} = 1 - 0.01672 \cos[0.9856(Julian\ Day - 4)] \tag{2-14}$$

with cosine in radians. The clear sky transmissivity, τ_{sw} (-), or fraction of extra-terrestrial solar radiation reaching the earth's surface under cloudless conditions, is computed as a function of elevation (Hingray et al. 2014):

$$\tau_{sw} = 0.75 + 0.00002\, z \tag{2-15}$$

where z (m) is the ground elevation of the golf course determined from a digital elevation model (DEM) with reference to *above sea level* (ASL). $R_{L\downarrow}$ and $R_{L\uparrow}$ are estimated as follows:

$$R_{L\downarrow} = \varepsilon_a \sigma \, T_a^4 \tag{2-16}$$

$$R_{L\uparrow} = \varepsilon_s \sigma \, T_s^4 \tag{2-17}$$

where ε_a (-) is the atmospheric emissivity which assumes an exponential atmospheric profile for temperature, pressure and humidity, σ (5.67×10^{-8} W·m^{-2}·K^{-4}) is the Stefan-Boltzmann constant and T_a (K) is the near surface air temperature. ε_a and ε_s are given by Brutsaert (1975) and Bastiaanssen et al. (1998), respectively:

$$\varepsilon_a = 1.24 \left(\frac{e_a}{T_a}\right)^{0.14286} \tag{2-18}$$

$$\begin{aligned} \varepsilon_s &= 1.009 + 0.047 \ln(NDVI) \quad (NDVI \geq 0) \\ \varepsilon_s &= 1.009 \quad (NDVI < 0) \end{aligned} \tag{2-19}$$

where T_a (K) is the near surface air temperature and e_a (mb) is the actual vapor pressure given by (Chow *et al*, 2013):

$$e_a = 6.11 \exp\left(\frac{17.27 \, T_d}{237.3 + T_d}\right) \tag{2-20}$$

where T_d (°C) is the dew point temperature.

In this study, thermal inertia is solved for twice using two distinct data sets and then using a θ retrieval process similar to that first proposed by Minacapilli et al. (2009). The first solution of thermal inertia is provided by Eqs. 2-1, 2-2, 2-3 and 2-4, which are solved simultaneously for incremental values of θ using real soil physical parameters obtained from soil samples. We refer to this thermal inertia parameter as P. The incremental values of θ *–as the independent variables in the solution of P–* are stored in matrix form by soil group. The second set of thermal inertia values are derived from remotely-sensed imagery and surface energy balance modeling (Eqs. 2-6 – 2-15)

with the solutions stored as rasters in the GIS environment. We refer to the remotely-sensed (thus spatially-distributed) estimation of thermal inertia as P_{rs}. Matching is later performed between the matrix and the rasters (P and P_{rs}, respectively) by retrieving the corresponding θ value from the matrix for every raster pixel of P_{rs}, resulting in a spatially-distributed map of θ. We herein refer to the remotely-sensed estimations of volumetric water content as θ_{rs} to distinguish from volumetric water content measured with a TDR soil moisture sensor (θ_{TDR}). The general workflow of the *PrISMM* methodology is displayed in Figure 2-1 with computational steps summarized in Table 2-1.

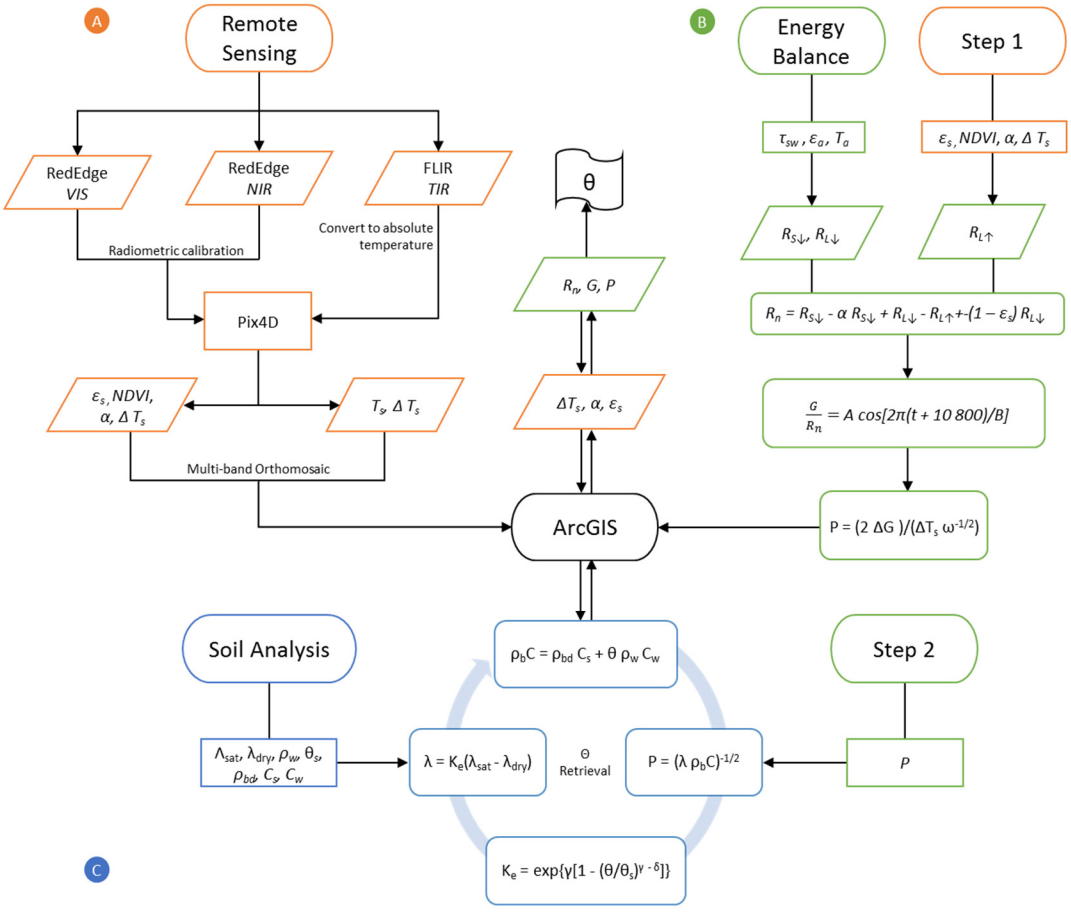

Figure 2-1 Precision Irrigation Soil Moisture Mapper (PriSMM) Methodology.

Table 2-1 Computational steps in *PrISMM* methodology.

Step	Symbol	Name	Unit	Equation
1.	P	thermal inertia	$J\ m^{-2}\ K^{-1}\ s^{-1/2}$	$P = (\lambda\ \rho_b C)^{-1/2}$
1.	λ	soil thermal conductivity	$W\ m^{-1}\ K^{-1}$	$\lambda = K_e(\lambda_{sat} - \lambda_{dry})$
1.	K_e	Kersten number	-	$K_e = \exp\{\gamma[1 - (\theta/\theta_s)^{\gamma - \delta}]\}$
1.	$\rho_b C$	soil heat capacity	$J\ m^{-3}\ K^{-1}$	$\rho_b C = \rho_{bd} C_s + \theta\ \rho_w C_w$
2.	NDVI	normalized difference vegetation index	-	NDVI = (NIR-red)/(NIR+red)
3.	$\propto$	albedo	-	$\alpha \simeq w_{\rho 1} r_{\rho 1} + w_{\rho 2} r_{\rho 2} + w_{\rho 3} r_{\rho 3} + w_{\rho 4} r_{\rho 4} + w_{\rho 5} r_{\rho 5}$
4.	ε_s	surface emissivity	-	$\varepsilon_s = 1.009 + 0.047 \ln(NDVI)$
5.	τ_{sw}	atmospheric transmissivity	-	$\tau_{sw} = 0.75 + 0.00002\ z$
6.	ε_a	atmospheric emissivity	-	$\varepsilon_a = 1.24(e_a/T_a)^{0.14286}$
7.	$R_{L\uparrow}$	outgoing longwave radiation	$W\ m^{-2}$	$R_{L\uparrow} = \varepsilon_s\ \sigma\ T_s^4$
8.	$R_{L\downarrow}$	incoming longwave radiation	$W\ m^{-2}$	$R_{L\downarrow} = \varepsilon_a\ \sigma\ T_a^4$
9.	d	earth-sun Distance	AU	$d/AU = 1 - 0.01672 \cos[0.9856(Julian\ Day-4)]$
10.	$R_{s\downarrow}$	incoming shortwave radiation	$W\ m^{-2}$	$R_{S\downarrow} = (G_{sc} \cos\varphi\ \ \tau_{sw})/d^2$
11.	R_n	net radiation	$W\ m^{-2}$	$R_n = R_{S\downarrow} - \propto R_{S\downarrow} + R_{L\downarrow} - R_{L\uparrow} - (1 - \varepsilon_s)\ R_{L\downarrow}$
12.	A	maximum G/R_n	-	$A = 0.0074\ \Delta T_s + 0.088$
13.	B	phase correction	s	$B = 1729\ \Delta T_s + 65{,}013$
14.	G	ground heat flux	$W\ m^{-2}$	$G = R_n\{A \cos[2\pi(t + 10\ 800)/B)]$
15.	P	thermal inertia	$J\ m^{-2}\ K^{-1}\ s^{-1/2}$	$P = (2\ \Delta G\ )/(\Delta T_s\ \omega^{-1/2})$
where,				
	$\propto$	surface albedo	-	
	γ	texture parameter	-	
	δ	shape parameter	-	
	C_s	solid phase heat capacity	$J\ kg^{-1}\ K^{-1}$	
	ρ_w	density of water	$kg\ m^{-3}$	
	G_{sc}	solar constant	$W\ m^{-2}$	
	C_w	liquid phase heat capacity	$J\ kg^{-1}\ K^{-1}$	
	S_r	relative water content	-	
	ω	radial frequency (24-hr)	s^{-1}	
	σ	Stefan-Boltzmann constant	-	
	ΔG	amplitude of LST heat flux	$W\ m^{-2}$	
	θ	actual volumetric SWC	$m^3\ m^{-3}$	
	λ_{sat}	saturated thermal conductivity	$W\ m^{-1}\ K^{-1}$	
	λ_{dry}	dry thermal conductivity	$W\ m^{-1}\ K^{-1}$	
	θ_s	volumetric saturated SWC	$m^3\ m^{-3}$	
	ρ_{db}	dry bulk density of soil	$kg\ m^{-3}$	
	ΔT_s	LST difference	K	
	T_a	air temperature	K	
	T_s	land surface temperature	K	
	φ	angle of incidence	rad	
	d	earth-sun distance	AU	
	z	elevation (msl)	m	

The remotely-sensed estimates of volumetric water content (θ_{rs}) are validated using actual volumetric water content values from a TDR soil moisture sensor (θ_{TDR}) for both calibration and quantifying the model accuracy. The data collection process is described in the following sections along with a description of the study area and results from site-specific soil analysis.

2.2. Study Area

This study was conducted during the fall of 2017 (October 12 – October 30) at Meadowbrook Park Golf Course (Meadowbrook) in Arlington, north central Texas, USA (Figure 2-2). Meadowbrook is located one mile east of downtown Arlington in Meadowbrook Park. This 9-hole course which opened in 1924 is the oldest in Arlington. The study area consists of small greens and narrow fairways lined with pecan trees, covering an area of approximately 0.09 km^2. Meadowbrook is characterized by gently sloping topography that abuts Johnson Creek on the western edge. The golf course is owned and operated by the City of Arlington (City). The site was selected due the City's continued commitment to water-conserving practices, its proximity to the University of Texas at Arlington (UTA), and a relatively undisturbed soil profile due to minimal land modifications over the intervening decades. Meadowbrook lies within the northern edge of Arlington Municipal Airport's Class D airspace with all flights conducted in accordance with FAA Part 107.

Meadowbrook consumes approximately 45 – 57 million liters (12 – 15 million gallons) of water annually. In an effort to all-but-eliminate the reliance on Arlington municipal water for irrigation, the City purchased and began installation of a water well in 2013 which taps the Paluxy aquifer. The groundwater is pumped and stored on-site in a holding pond whereby a pumping station draws water into the course's irrigation system which is distributed through 162 sprinkler heads. Prior to this study, irrigation was conducted at the superintendent's discretion and with the aid of

Texas ET Network (TexasET), provided by Texas A&M AgriLife Extension - Irrigation Technology Program. The primary disadvantage of *TexasET*, which uses the standard Penman-Monteith, is that it provides point estimates for potential evapotranspiration (ET_0) based on a sparse network of weather stations. This leads to a uniform irrigation depth which results in some areas receiving more water than required while other areas, especially topographic high points, do not receive enough. It is hypothesized that the spatially-distributed application of irrigation water could reduce total water use while maintaining healthy and playable turfs. To achieve this goal of spatially-distributed irrigation management, the radius of influence of each sprinkler head is used to delineate the golf course into several irrigation management zones in which sprinklers may be operated independently as required.

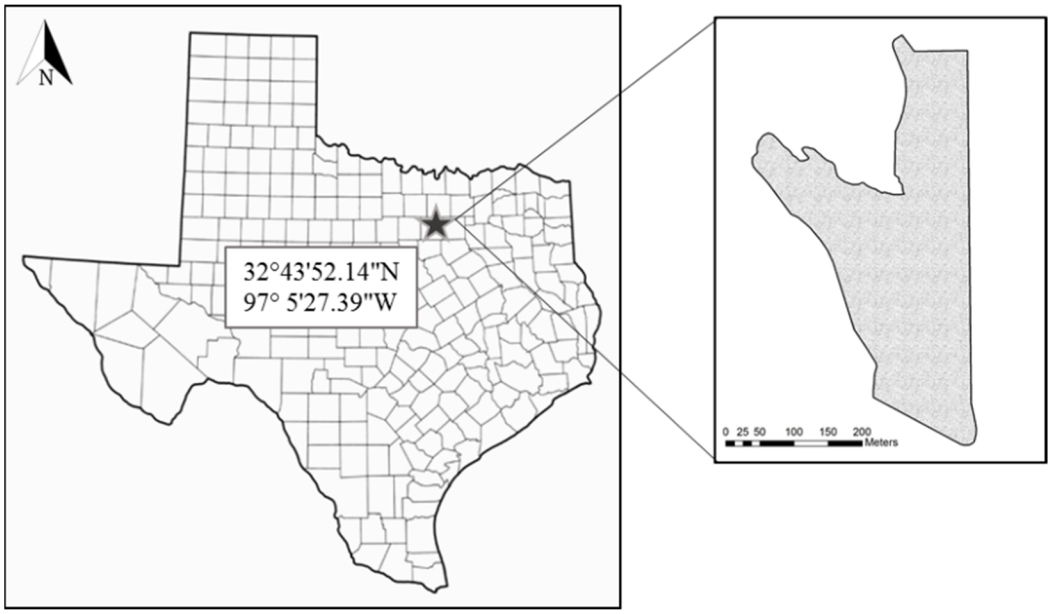

Figure 2-2 Location of study area in north central Texas.

2.3. Soil Analysis

The thermal inertia approach was used in this investigation which requires detailed soil characterization of the site. A series of *in situ* and laboratory experiments was therefore conducted to determine soil physical properties of the study area (soil type, texture, mineral composition, bulk density and thermal properties). This opportunity was also used to perform site-specific calibration on a FieldScout TDR 300 soil moisture meter (TDR) using gravimetric sampling. ArcGIS was used to generate ten randomly-placed sample points within the boundaries of the study area for sample collection. The sample locations were wetted to different degrees, followed by a period reading from the TDR using 7.6 cm rods with 3.3 cm spacing. The soil column was then extracted using a 25 cm long core sampler with an inner sleeve diameter of 15 cm. The samples were sealed in plastic bags and placed on ice for laboratory analysis. The sand-cone method was also used to determine the volume and bulk density of the soil samples (ASTM 2007).

Site-specific calibration was performed for the TDR by developing a relation between the TDR sensor's period readings *against* actual VWC. Immediately after returning from the field, the soil cores were removed from the plastic bags, weighed on a precision scale, and oven dried at 105°C for 48 hours. The samples are then reweighed to determine GWC:

$$GWC = \frac{m_{wet} - m_{dry}}{m_{dry}} \tag{2-21}$$

where m_{wet} is the mass of the bulk sample and m_{dry} is the mass of the dry sample. The VWC of the sample (θ_v) is the volume of the water divided by the total volume of the sample (V_T) but is similarly calculated from GWC:

$$\theta_v = GWC \times \frac{\rho_{bd}}{\rho_w} \tag{2-22}$$

where ρ_w (998 kg/m^3) is the density of water at 20°C and ρ_{bd} (kg/m^3) is the dry bulk density given by:

$$\rho_{bd} = \frac{m_{dry}}{V_T} \tag{2.23}$$

where the mean measured value of ρ_{bd} is 1,260 kg m^{-3}. Measured period readings were next plotted *against* the corresponding θ_v calculations from equation 2-22 for regression analysis to produce the following equation:

$$\theta = 0.0002\,\Gamma - 0.3105 \tag{2.24}$$

where θ is the calibrated soil volumetric water content (m^3 m^{-3}) and Γ is the period (μs). A fully-saturated sample (not included in regression) was used to determine the saturated soil water content, θ_s (0.57). The calibrated TDR results are provided in Figure 2-3.

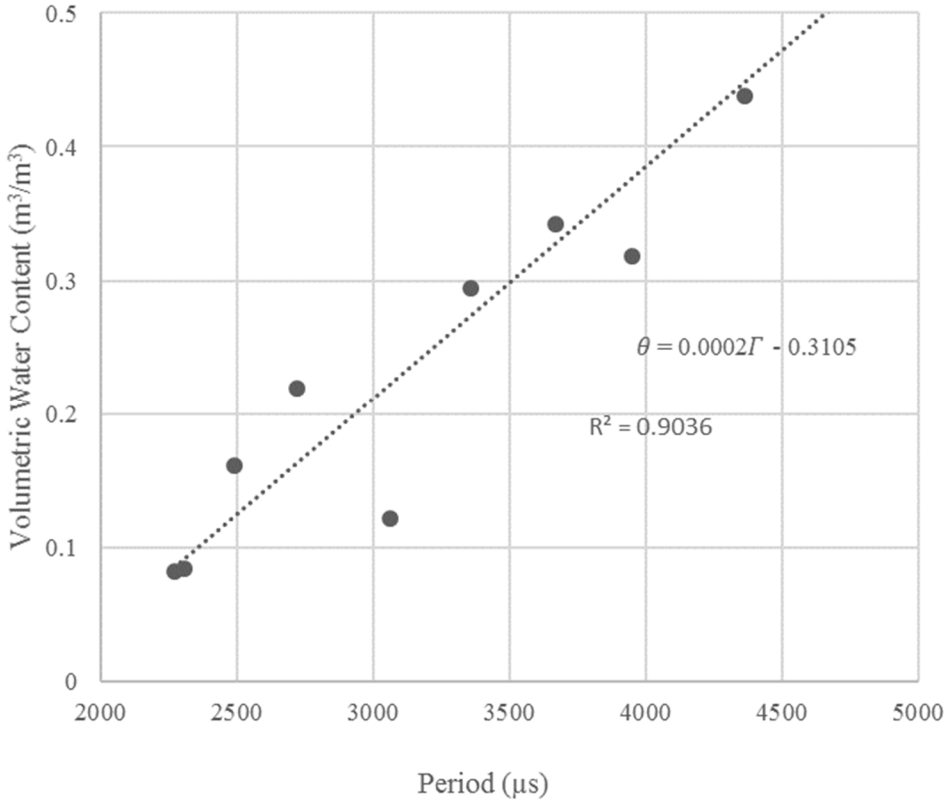

Figure 2-3 Calibration graph for FieldScout TDR 300 soil moisture sensor for loamy sand.

Textural analysis was also performed using the sieve and hydrometer method (Gee and Bauder 1986). Per USDA classification, the texture of the surface soil horizon is composed of loamy sand (NRCS 1986) with a mass fraction of sand, silt and clay of 0.85, 0.05, 0.10 g g^{-1}, respectively. The soil textural triangle confirms that the predominant soil type at Meadowbrook is loamy sand (Figure 2-4). A *KD2 Pro* equipped with a *TR-1* thermal conductivity/resistivity sensor was used to determine the mean values for λ_{sat} (0.896 W m^{-1} K^{-1}) and λ_{dry} (0.220 W m^{-1} K^{-1}). A *SH-1* dual-needle thermal diffusivity and specific heat sensor was used to measure the mean value of C_S (975 J kg^{-1} K^{-1}). The soil parameters were then used to carry out the calculations in Step C of the *PriSMM* methodology as shown in Figure 2-1.

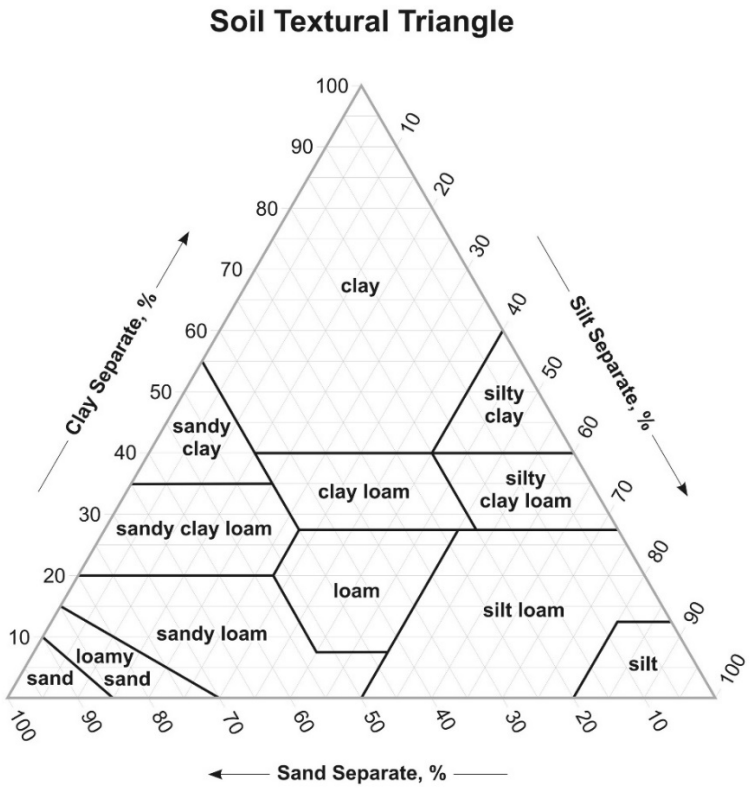

Figure 2-4 Soil textural triangle and textural classes (*Source*: USDA—National Resources Conservation Service).

2.4. UAV Platform

In order to derive θ_{rs}, an unmanned aerial vehicle (UAV) equipped with multispectral sensors is utilized. The UAV platform used in this study, *MavAir One*, is a powerful remote sensing octocopter with a 24-pound maximum takeoff weight and payload including a multispectral sensor array. *MavAir One*'s custom spectral bands were modeled after *RapidEye* satellites to provide critical calibration/validation data for global downscaling with applications in agriculture, forestry, oil and gas exploration, mining and water resources management. *MavAir One* is also equipped with a high-resolution thermal camera used for water-energy balance modeling. *MavAir One*'s advanced flight computer is integrated with three GPS units and two IMUs for the greatest accuracy and positioning. The flight computer is controlled by either a 2.4 GHz handheld transmitter or laptop.

A *Micasense RedEdge*^{TM} camera supplies spectral data on five discrete narrow bands, including blue (ρ_1), green (ρ_2), red (ρ_3), red edge (ρ_4), and NIR (ρ_5) with an image array of 1280 x 960 pixels (Micasense 2015). Derived multi-band orthomosaics are used to develop vegetation indices such as NDVI. The *RedEdge*^{TM} reflectance values are radiometrically calibrated to ensure that time-series data accurately reflect changes in vegetation as opposed to changes in lighting conditions. To overcome variations in ambient light occurring day-to-day and also during flight, two instruments are employed: (1) a calibrated reflectance panel (CRP) and (2) a down-welling light sensor (DLS). Immediately before and immediately after each flight, an image of the CRP is captured on all five *RedEdge*^{TM} bands in which the albedo of the target is known. The DLS is installed on the top of the aircraft and points upward towards the sky. For each camera triggering event, solar irradiance (W m^{-2}) is instantaneously recorded and embedded within the metadata of each band. Both the CRP and DLS are then used in post-processing to correct for changing illuminations during flight. (Micasense 2015). Corrections are based on solar irradiance and sensor properties (gain/bias settings for each band). Before mosaicking, all images are transformed to a

theoretically common illumination condition, therefore reducing variations in reflectance or brightness for maximum accuracy and repeatability.

A *FLIR Vue Pro R* provides non-contact, calibrated, radiometric measurements to derive temperature estimates for each pixel. The thermal imager is an uncooled VOx micro-bolometer which detects longwave infrared energy in the 7.5–13.0 μm thermal spectral range with an image array of 640 x 512 pixels. Surface temperatures are automatically computed using a fixed emissivity of unity. Raw sensor data are recorded as grayscale bands and stored in uncompressed 14-bit TIFF format. Surface temperature was also measured using a handheld *Fluke ST2* thermal infrared gun with ±1% accuracy. The gun was pointed at a 45° angle to the surface at a distance of 1 m, resulting in a ground footprint of approximately 0.25 m^2. IR gun measurements were used to calibrate/validate the airborne TIR images, assuming a linear relationship between thermal brightness and land surface temperature for both morning and midday flights. Images are imported into *Pix4D Mapper Pro* where raw thermal values are converted to absolute temperature. *MavAir One* sensor specifications are shown in Table 2-2 UAV advanced remote sensors with specifications.

Table 2-2 UAV advanced remote sensors with specifications.

Sensor	Resolution	Name	Symbol	Bandwidth	Wavelength (μm)
Sony α6000	6000 x 4000	Blue	-	Broad	0.45-0.52
	6000 x 4000	Green	-		0.52-0.60
	6000 x 4000	Red	-		0.63-0.69
Micasense RedEdge™	1280 x 960	Blue	ρ_1	Narrow	0.465-0.485
	1280 x 960	Green	ρ_2		0.550-0.570
	1280 x 960	Red	ρ_3		0.663-0.673
	1280 x 960	Red Edge	ρ_4		0.712-0.722
	1280 x 960	Near Infrared	ρ_5		0.820-0.860
FLIR Vue Pro R	640 x 512	Thermal	ρ_6	Broad	7.5-13.5

All camera shutters are integrated with *MavAir One*'s onboard GPS and IMU and record latitude, longitude, elevation and orientation (pitch, yaw and roll) of the aircraft for every camera trigger event in a process known as *geotagging*. The images are later aligned and processed to generate orthophotomaps for each spectral data set which are georeferenced in NAD83 (HARN) / Texas North Central (ft US). When the multispectral maps are imported into a Geographic Information System (GIS), the various spectral ranges, or bands, can be resampled and overlaid into composite orthophotomaps and analyzed for spectral signatures associated with thermal inertia and volumetric water content. The remotely-sensed products include the following orthomosaics: (1) VIS-NIR (2) TIR, (3) NDVI, (4) α, (5) ε_s, (6) G, P, and θ_{rs}.

2.5. Data Collection

UAV data were collected twice per day during the fall of 2017 (12 October—30 October) on 6 days. Each data set consists of two flights collected on the same day, including a morning flight and a midday flight. In this study, flights are conducted 30 minutes prior to official sunrise when surface heat fluxes are negligible, thus serving as a starting point for optical and thermal imagery collected later the same day (within 1 h of solar noon). A total of 12 flights were conducted resulting in 6 sets of input data for the *PriSMM* model. All flights were automated through waypoint navigation software using the same flight plan for all missions, thus eliminating variability in altitude and coverage. Takeoffs and landings were performed manually using a transmitter while automated waypoint navigation was conducted using a laptop and a 2.4 GHz Bluetooth datalink, consisting of an air and ground end for wireless transmissions. Mission altitude was 70 m *above ground level* (AGL) with a forward speed of 7 m s^{-1}. Vertical and horizontal overlap of photos was 80 percent. Ground sampling distance of the *RedEdge*^{TM} and *FLIR Vue Pro R* were 4.6 cm and 8.6 cm, respectively. Table 2-3 summarizes the UAV flights and atmospheric conditions.

Table 2-3 Meteorological conditions for each flying day.

Date	Solar Noon CDT	Temp °C	Dew Pt. °C	φ rad	Humidity	Visibility km	Wind Speed kts	Sky
10/12/2017	13:14	28.1	12.5	0.866	40%	> 10	5	Clear
10/17/2017	13:13	23.9	12.2	0.833	38%	> 10	8	Clear
10/18/2017	13:13	25.6	6.7	0.827	37%	> 10	11	Clear
10/28/2017	13:12	22.8	7.2	0.784	18%	> 10	8	Clear
10/29/2017	13:12	23.0	3.3	0.723	14%	> 10	12	Clear
10/30/2017	13:12	22.2	33.8	0.760	28%	> 10	3	Clear

Immediately following each midday flight, intensive ground truthing was performed over the study area using a FieldScout TDR 300 (TDR) soil moisture meter. The TDR was selected for its ability to quickly and reliably provide accurate VWC estimates for surface soil layers (Brevik 2012). TDR readings by day ranged from 55 to 518 per data set. For the first TDR survey on October 12, readings are relatively uniform, with single readings collected every fifteen paces. Due the highly-variable nature of soil moisture distribution, samples were later collected in clusters of three to twelve (3 × 3 m plots) for the remaining five collection dates. In this way, stronger patterns of VWC variability should emerge with anomalies or outliers more easily identified. The TDR includes a data logger and GPS which records geo-referenced period readings in the logger's storage file system. Figure 2-5 displays the combined ground truthing for all six events, totaling 1,300 TDR readings. Six sets of ground truthing data were imported into ArcGIS as point features for *PrISMM* model validation.

Figure 2-5 Spatial distribution of soil moisture samples from FieldScout TDR 300.

Chapter 3

Results

Combining high resolution thermal and multispectral orthophotomaps with surface energy balance modeling and soil physical parameters produces spatially-distributed volumetric water content maps which reveal irrigation patterns that cannot be detected using traditional *in situ* or remote sensing methods. The *PrISMM* model is executed for data collected on six days during the fall of 2017 in which predicted (remotely-sensed) estimates of volumetric water content (θ_{rs}) are compared against actual (measured with TDR sensor) values of volumetric water content (θ_{TDR}). Spatially-distributed raster data sets of land surface temperature (T_s), *normalized difference vegetation index* (NDVI), albedo (grass and soil combined) (α), surface emissivity (ε_s), net radiation (R_{net}), ground heat flux (G), thermal inertia (P) and θ_{rs} are attained for each flying day with resolutions of 8.6 cm (Figure 3-1). *PrISMM* soil moisture maps are displayed *against* measured VWC in Figure A-1 throughFigure A-6 of Appendix-1.

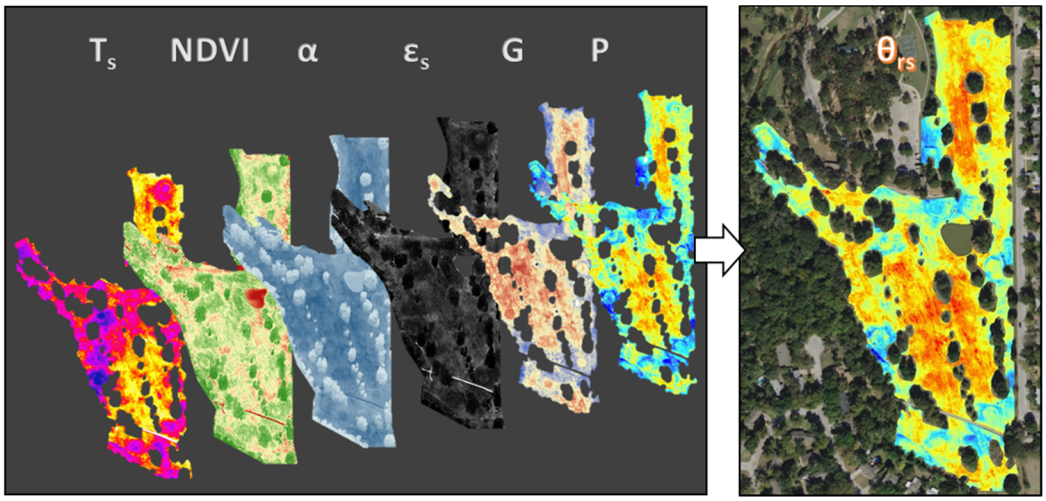

Figure 3-1 Raster layers generated using *PrISMM* methodology for October 25, 2017: (from left to right); T_s, NDVI, α, ε_s, G, P, and θ_{rs}.

Because the objective is to determine irrigation requirements for the golf course, an image processing algorithm is applied to each raster data set to remove all non-soil/grass features such as trees, concrete, a pond, built structures, golf carts and patrons of the golf course. In this way, averages for spatially-distributed calculated parameters exclusively represent the intended feature–*turfgrass*, as shown in Table 3-1. As this study was conducted in the mid-fall, the maximum solar zeniths steadily decreased from 49.6° to 43.3° causing some areas of turfgrass to be perpetually covered in shadows from tall trees. These shadowed regions are reflected in the model as false wet zones and are thus removed in pre-processing to prevent systematic bias.

Table 3-1 Average spatially-distributed calculated parameters for each flying day.

Date	$^{*}T_s$ (° C)	NDVI (-)	ε_s (-)	α (-)	G (W m^{-2})	P (J m^{-2} K^{-1} $s^{-1/2}$)	Θ_{rs} (m^3 m^{-3})
10/12/2017	27.58	0.61	0.99	0.26	48.16	1332.72	28.47
10/17/2017	26.49	0.61	0.98	0.26	39.05	1354.03	29.59
10/18/2017	28.96	0.60	0.99	0.27	38.75	1383.56	31.17
10/25/2017	27.34	0.59	0.98	0.27	40.07	1332.91	28.48
10/29/2017	24.84	0.59	0.98	0.28	47.51	1319.83	27.80
10/30/2017	24.69	0.59	0.98	0.28	62.02	1308.76	27.23

* Temperature recorded during midday flight (approximately solar noon).

For the calculation of ΔT_s, Atmospheric corrections to the TIR imagery were applied with a built-in radio-transfer model within the FLIR hardware. As reported by Hoffman et al. (2016), the image processing software was unable to mosaic the early morning TIR images due to the relative homogeneity of surface temperatures throughout the golf course. To successfully orthorectify a set of photos, the software must first identify key points. Using the camera location, orientation and camera properties such as resolution and focal length, the software projects a line from the camera through the key point and repeats for all overlapping photos in the process of triangulation. Because key points for TIR imagery are composed of temperature estimates as pixels, the relatively uniform temperature field at early morning prevented sufficient key point density from being established.

Similar to Hoffman et al., the mean temperature of the turfgrass was used for the initial surface temperature, which was established from individual TIR images captured at an elevation of 70 m. Calibrated thermal orthophotomaps derived from early-morning and midday TIR imagery resulted in ΔT_s values ranging from 5.1 to 21.6 °C with the smallest changes associated with ponded water and the highest associated with dry soils.

Observed solar radiation data was provided by the National Weather Service (NWS) of Fort Worth, with the weather station located approximately 22 km WNW of Meadowbrook. Observed values were compared with calculated for the time at solar noon for validation purposes using equations 2-13 through 2-15. For the data sets occurring on October 12th, 17th and 18th, the calculated values of $R_{s\downarrow}$ yielded excellent agreement (±1%) with the observed (see Figure A-7 of Appendix A). For the dates of October 25th, 29th and 30th, however, equations 2-13 through 2-15 over-predicted $R_{s\downarrow}$ by as much as 22%. The departure of the calculated from the observed values is likely a consequence of an atmospheric scattering parameter not accounted for by the clear sky transmissivity equation, 2-15. For this study, the NWS values were used to determine net radiation, however, it is recommended that a four-component net radiometer or pyranometer be installed at the site for the greatest possible accuracy.

As previously noted, ground truthing was accomplished using a calibrated TDR soil moisture sensor. Georeferenced period readings were collected immediately after each midday flight, ranging from 55 to 518 readings per data set, with 1,300 readings in total. For the first TDR survey on October 12, readings are relatively uniform, with single readings collected every fifteen paces. Due to the highly-variable nature of soil moisture distribution, samples were later collected in clusters of three to twelve (3 × 3 m plots) for the remaining five collection dates. Some wet and dry spots were present in each data set due to deficiencies in the irrigation sprinkler system which served as quality controls/boundary conditions for the *PrISMM* model.

Soil descriptions were also recorded during TDR surveys in which four soil classes were identified by sight and texture, including (a) loamy sand, (b) sand, (c) sandy loam, and (d) silty clay loam. All recorded observations were imported into the ArcGIS environment to delineate and refine the existing SSURGO soil distributions, as shown in Figure 3-2.

Figure 3-2 Refined soil classification map from field survey

Loamy sand is the predominant soil type and is present throughout the site. Sandy loam is much less common and is characterized by a dark gray color with a sandy texture, found near the

outer edges of the golf course. Silty clay loam is found at topographic high points throughout the course, possibly indicating that it was locally excavated and redistributed to appropriate the topology of the course. For instance, the main strip of silty clay loam in the northern region of the map distinctly separates two fairways. All putting greens and tee boxes are built on sand characterized by high porosity and infiltration rates. Updated soil classifications were then used to fine-tune the model calibration.

The maintenance standards of the golf course require mowing every three to six days leading to a grass length of 3 to 10 mm, depending on the stage within the growing season. Due to the relatively small size of the golf course, the tee boxes, fairways and roughs were all mowed to the same length. For this study, grass was assumed to be homogenous in terms of density and distribution. This assumption allowed for the application of a constant attenuation factor for modeling mechanical resistance with respect to the surface temperature of the soil.

Goodness-of-fit statistics were computed to evaluate the degree of association between the actual *versus* predicted values of VWC, including the coefficient of correlation (r), coefficient of determination (R^2), root mean square error (RMSE) and mean absolute error (MAE), summarized in Table 3-2.

Table 3-2 Actual vs. predicted goodness-of-fit statistics.

Date	# of TDR Measurements	r	R^2	RMSE	MAE
10/12/2017	194	0.8281	0.6858	0.0414	0.0331
10/17/2017	100	0.8856	0.7843	0.0522	0.0427
10/18/2017	116	0.9088	0.8260	0.0557	0.0416
10/25/2017	55	0.8924	0.7963	0.0536	0.0449
10/29/2017	518	0.8691	0.7553	0.0351	0.0261
10/30/2017	317	0.8174	0.6681	0.0357	0.0267
Total	1300	0.8863	0.7855	0.0408	0.0308

For R^2 values, the minimum (0.67) and maximum (0.83) values were obtained on October 30th and October 18th, respectively. The mean R^2 value for all six dates was 0.79. For RMSE values ($m^3\ m^{-3}$), the minimum (0.04) and maximum (0.06) values were obtained on October 29th and October 18th, respectively. The mean RMSE for all six dates was 0.04. For MAE values ($m^3\ m^{-3}$), the minimum (0.03) and maximum (0.04) values were obtained on October 29th and October 18th, respectively. The mean MAE for all six dates was 0.03. Figure 3-3 illustrates a one-by-one scatter plot of the actual *versus* predicted VWC values for all six dates combined with one-by-one scatter plots of the actual *versus* predicted VWC values for the six individual dates appearing Figure A-8 of Appendix A. Overall, the results indicate that the *PrISMM* model has the ability to estimate VWC with good accuracy. Model performance is discussed in greater detail in Section 3.1 with recommendations for operational use discussed in Section 3.2.

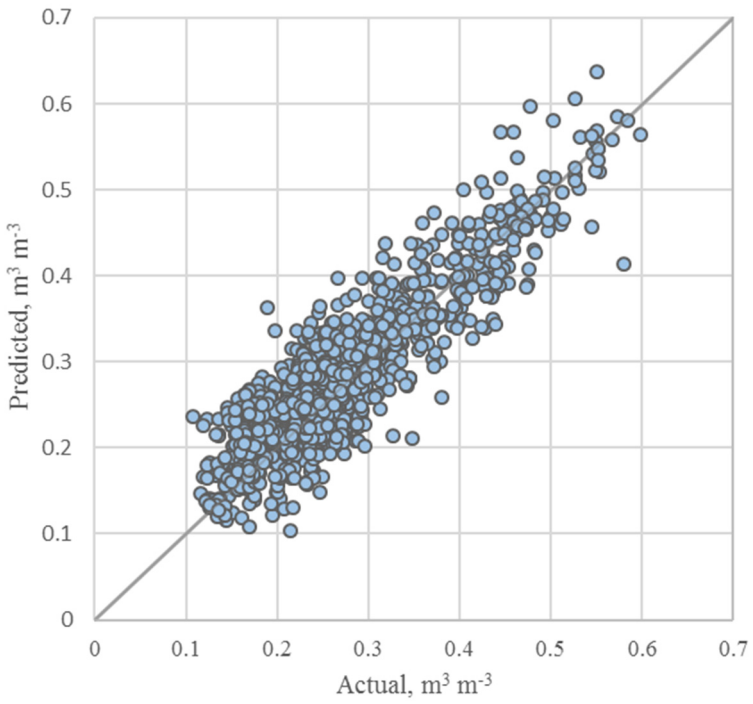

Figure 3-3 Scatter plot of actual vs. predicted Volumetric Water Content ($m^3\ m^{-3}$) for October 12 through October 30, 2017.

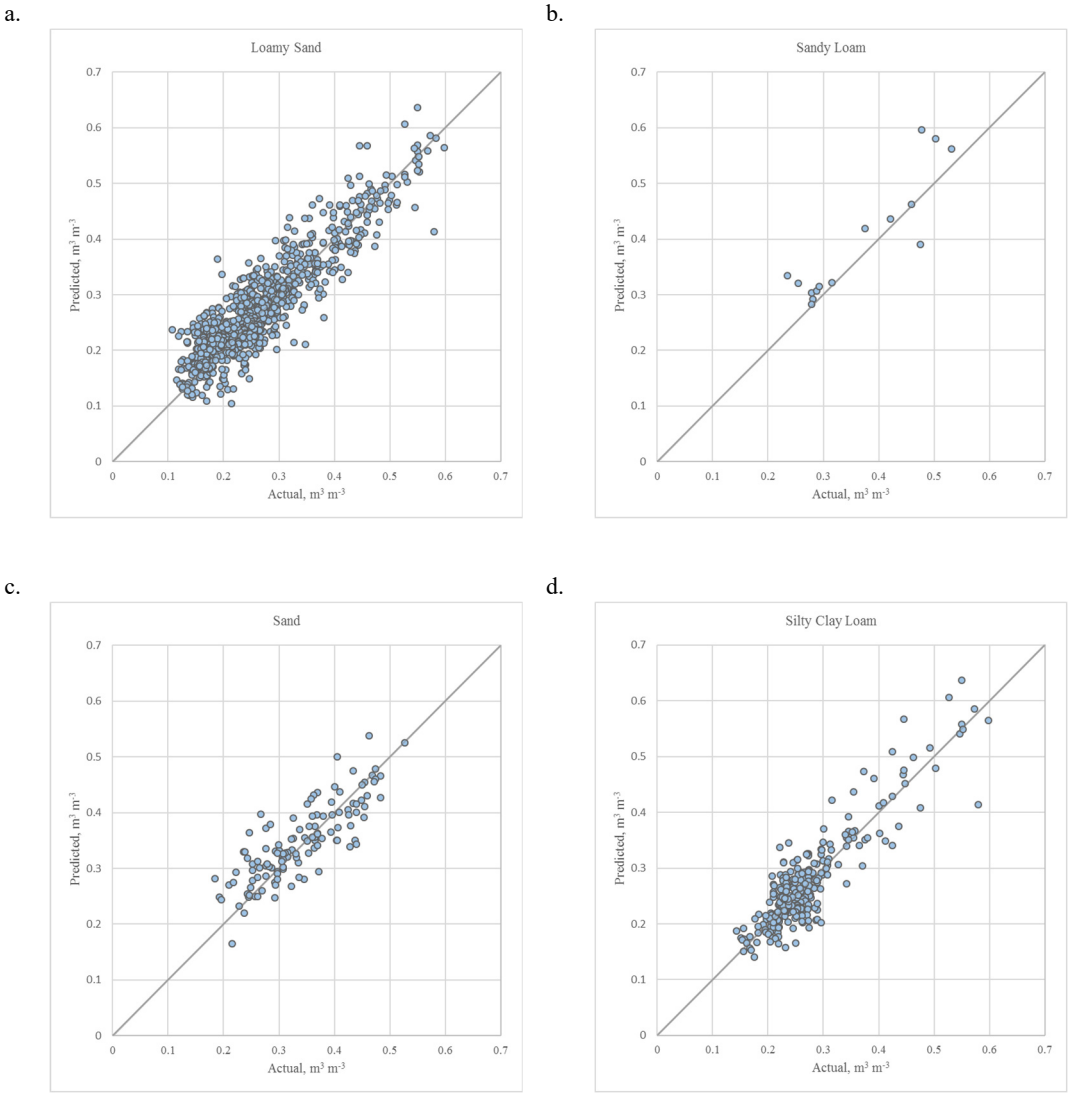

Figure 3-4 Mean volumetric water content ($m^3\ m^{-3}$) by soil type: (a) loamy sand, (b) sandy loam, (c) sand, and (d) silty clay loam.

The goodness-of-fit statistics were also separated by soil groups for comparison (Table 3-3). The highest R^2 value was associated with silty clay loam (0.81), followed by loamy sand (0.77), sandy loam (0.86) and sand (0.57). The markedly reduced performance in predicting VWC for sand could be associated with a number of factors. First, the relatively high rate of infiltration of sand means that the VWC will remain less constant. Due to the lag between the time of the midday flight and the time which the TDR reading is taken, actual SMC may fluctuate. The variability of SM is also increased for sand, as observed during TDR readings. Due to the importance of the putting greens, it is important to preserve their integrity. As such, soil cores were not removed during site-specific soil analysis with the physical and thermal properties estimated instead. It is believed that accuracy of VWC prediction could be increased by performing the soil analysis for the sands and also reducing the time between the collection of the remotely-sensed data and the TDR readings. A future study will take these aspects of sand into account.

Table 3-3 Actual vs. predicted goodness-of-fit statistics by soil group.

Date	# of TDR Measurements	r	R^2	RMSE
Sand	122	0.7564	0.5721	0.0447
Loamy Sand	841	0.8782	0.7712	0.0415
Sandy Loam	15	0.8639	0.7463	0.0555
Silty Clay Loam	322	0.8973	0.8052	0.0361

3.1. Discussion

Residual histograms of the actual *versus* predicted VWC for the six different dates are shown in Appendix A in Figure A-9 with a combined histogram of residuals shown in Figure 3-5. As shown in Figure 3-5, the combined residuals are centered on the origin and do not indicate significant systematic errors. Statistics for the residuals are summarized in Table 3-4 with the number of TDR readings for each collection event.

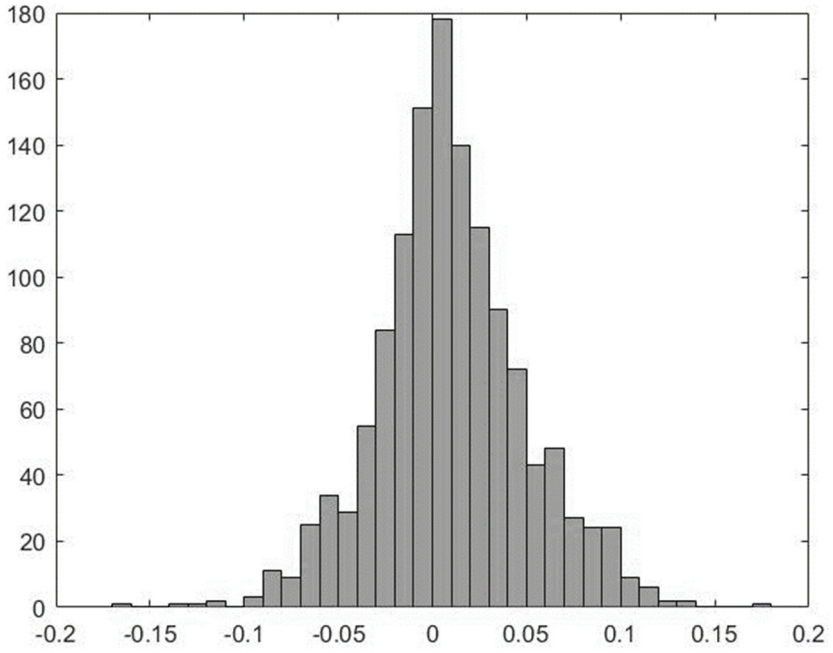

Figure 3-5 Histogram of actual vs. predicted Volumetric Water Content (m^3 m^{-3}) for October 12 through October 30, 2017.

Analysis of the mean residuals does not reveal any significant case of model bias as both negative and non-negative values are close to zero. For all six events, the minimum and maximum residual (m^3 m^{-3}) was -0.17 and 0.17 (range of 0.34), respectively, both occurring on October 18th. It was originally hypothesized that as the sample population of TDR measurements increased, the overall range of residuals would also increase, implying that the largest range of residuals should have occurred on October 29th (529 readings). At least for the data sets below, no immediate connection can be made between the number of TDR readings and model errors, suggesting that approximately 100 evenly-distributed or clustered (3 × 3 m) TDR measurements should be sufficient for validation of the *PrISMM* model.

Table 3-4 Residual statistics.

Date	# of TDR Measurements	Min	Max	Range	Mean	Median	Std. Dev.
10/12/2017	194	-0.0891	0.1082	0.1973	-0.0019	0.2835	0.0415
10/17/2017	100	-0.0976	0.1225	0.2201	0.0239	0.0255	0.0467
10/18/2017	116	-0.166	0.1741	0.3401	0.0203	0.0188	0.0521
10/25/2017	55	0.1371	0.0847	0.2218	-0.0147	-0.0250	0.0520
10/29/2017	518	-0.0956	0.1391	0.2347	0.0101	0.0075	0.0337
10/30/2017	317	-0.0936	0.1042	0.1978	0.0117	0.0078	0.0338
Total	1300	-0.1660	0.1741	0.3401	0.0097	0.0075	0.0397

A residual plot of the six combined dates is provided in Figure 3-6 while residual plots for individual dates are provided in Figure A-10 of Appendix A.

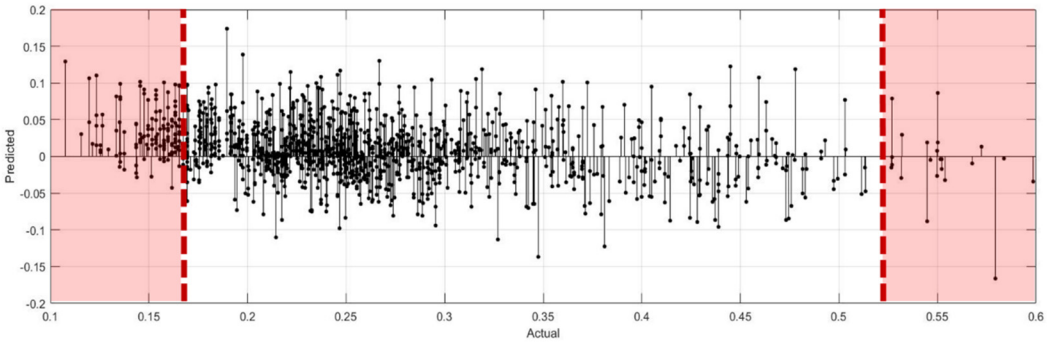

Figure 3-6 Residuals of actual vs. predicted volumetric water content ($m^3\ m^{-3}$).

Residuals for the combined dates are normally distributed for actual VWC ($m^3\ m^{-3}$) values greater than 0.17; however, for actual values below 0.17, the *PrISMM* model tends to overestimate VWC. The difficulty in estimating thermal inertia for low moisture contents has been documented elsewhere (Tarnawski and Leong 2000; Lu et al. 2007; Minacapilli et al. 2009). Minacapilli et al. for instance reported more scattered predictions of VWC below 0.15 $m^3\ m^{-3}$. This phenomenon is attributed to the relationship between the soil thermal conductivity (λ) and soil water content (θ), implicit in equations 2-1 through 2-4. For lower moisture contents, water molecules are more tightly

bound to soil particles; as θ increases in the dry domain, the water film continues to build on the particle surface, accompanied by a considerably smaller increase in λ (Lu et al. 2007). As the film continues to thicken, the water forms a bridge between soil particles and λ begins to increase rapidly. For mid-values of moisture content (0.17 – 0.50 m^3 m^{-3} in this study), the $\lambda(\theta)$ relationship is assumed to be linear. As the soil approaches saturation, however, the $\lambda(\theta)$ relationship becomes largely dependent on the displacement of air by water in which θ continues to increase with a more gradual increase in thermal conductivity; thus, the $\lambda(\theta)$ relationship tends to resemble an s-curve. In terms of operability of the *PrISMM* model, the difficulty in estimating θ (m^3 m^{-3}) for particularly low and high values is not considered to be problematic. The *PrISMM* model accurately detects the thresholds for $\theta_{rs} \leq 0.17$ and $\theta_{rs} \geq 0.50$ and flags these pixels as excessively dry or excessively wet, respectively. As later discussed in Section 3.2, precision irrigation management decisions are determined for the θ_{rs} domain within 20% of *field capacity*, or, approximately 0.17 to 0.54 m^3 m^{-3}.

Due to the general tendency of soil moisture to decrease throughout the day, the residuals are also plotted against the time in which the TDR readings are taken. It is hypothesized that as the time between θ_{rs} and θ_{TDR} increases, the magnitude of residuals will increase. The data set on October 29th, 2017 contained the largest lag time (1.7 – 4.27 h) between the remotely-sensed data and ground truthing data due to the large number of TDR readings (518). Figure 3-7 shows the predicted *minus* actual VWC *versus* time between θ_{rs} and θ_{TDR} for October 29th, 2017. For this event, no significant trends in VWC estimate errors and lag time are present. In order to more fully understand the relationship of these errors with lag time, an in situ TDR sensor may be installed on site to quantify the temporal aspects of VWC. Again, 100 TDR readings should be sufficient in quantifying the accuracy of the *PrISMM* model; therefore, provided that TDR readings are collected immediately after the midday flight, these lag errors are not expected to be significant.

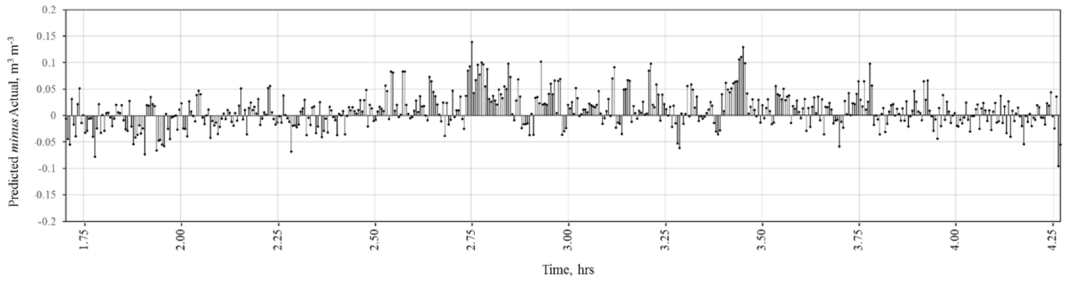

Figure 3-7 Predicted *minus* actual VWC ($m^3\ m^{-3}$) *versus* time between θ_{rs} and θ_{TDR}, October 29th, 2017.

In order to test the response of remotely-sensed estimates of θ_{rs} to individual irrigation and/or rain events, the *PrISMM* modeling domain was delineated into irrigation management zones to compute zonal statistics for each zone. The current irrigation system at Meadowbrook consists of 86 stations with two sprinkler heads each for a total of 162 sprinkler heads. Although stations may be operated independently, irrigation at Meadowbrook is currently divided into three irrigation management zones, i.e., (a) greens, (b) tee boxes and (c) fairways and roughs. This means, for example, that if VWC is insufficient for a stretch of fairway, all fairways and roughs will be irrigated the following night for equal time intervals. Similarly, if the entire lower half of the golf course is considered too dry but the top half satisfactory, the entire golf course will be irrigated the following night, albeit using independent time intervals per management zone. Figure 3-8 Irrigation management zones by grass type: (a) green, (b) tee box, (c) fairway, and (d) roughs.Figure 3-8 displays the current irrigation management zones by grass type: (a) green, (b) tee box, (c) fairway, and (d) roughs.

Figure 3-8 Irrigation management zones by grass type: (a) green, (b) tee box, (c) fairway, and (d) roughs.

The average θ_{rs} (%) values for each irrigation management zone are depicted in bar charts by date in Figure 3-9. For zones in which irrigation is conducted within the previous 12 h, the bars are marked as either *irrigated by sprinkler head* or *watered by hand* (hand watering is usually performed during daylight hours by visually identifying dry areas). Rainfall events were recorded at Arlington Municipal Airport (KGKY) which included Oct. 10 (0.13 in), Oct. 15 (0.01 in), Oct. 20 (0.01 in), and Oct. 22 (0.92 in). There are two sets of consecutive dates including Oct. 17th – 18th and Oct. 29th – 30th.

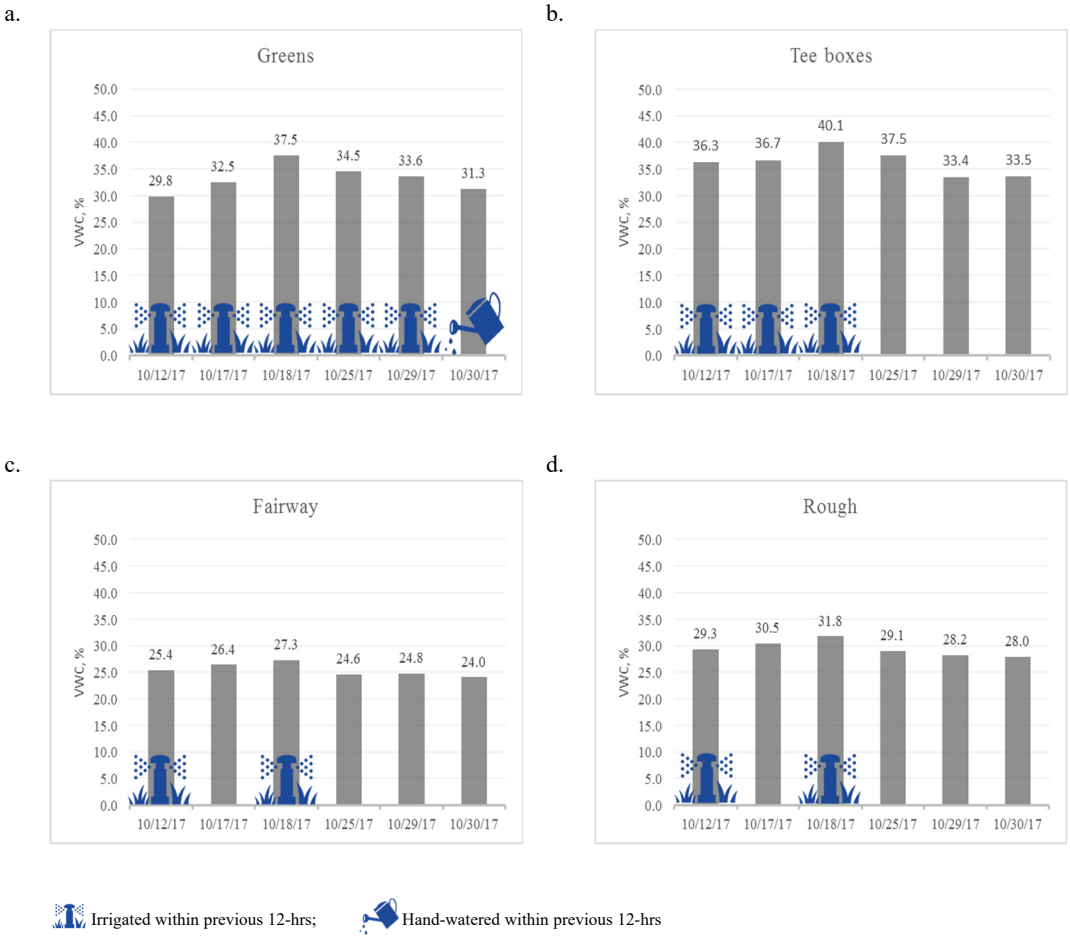

Figure 3-9 Mean volumetric water content (m^3 m^{-3}) by grass type and date: (a) greens, (b) tee boxes, (c) fairway, and (d) rough.

The response of θ_{rs} to rainfall was not evident for the selected dates, most likely due to the large gap between observed rainfall and data collection and the relatively small precipitation amounts. Due to the high infiltration rates of the greens and tee boxes (sand + organics) and higher standards for playability and vigor, the frequency of irrigation is significantly higher than for other surfaces. One observable response includes the slight decrease in VWC (%) of the greens from Oct. 29th – Oct. 30th where VWC remains relatively constant for the other surfaces. This is likely due to the lower intensity and precision (hence less water) of hand watering. For all four playing surfaces, VWC increases from Oct. 17th – 18th which is consistent with the irrigation pattern. Tee boxes are slightly higher in moisture content than greens despite the green's more frequent irrigation. This is likely due to the smaller sand fraction in the tee boxes which is by design. The roughs are also slightly higher in VWC than the fairways of which both surfaces are irrigated simultaneously. This is likely due to the tendency of ponded water to collect in the roughs. It is expected that as the number of consecutive data sets increase, and with more irrigation variability, stronger correlations between the response of θ_{rs} to rainfall and irrigation patterns will emerge.

3.2. Recommendations for Operational Use

The overall objective in the irrigation of turfgrass is to maintain *plant available water* (the difference between *field capacity* and *permanent wilting point*) at or above 50% for the longest duration with minimal loss from drainage or runoff (Murphy 2002). In order for *PrISMM* to drive a time-based irrigation system, irrigation management zones must be delineated by soil texture and rooting depth. The derived VWC maps are used to determine the percentage of *plant available water* (in/ft) at the time of the midday flight. It should be noted that optimal growth and plant health is typically observed between 50 to 80% of *plant available water* with severe symptoms of drought becoming apparent at 20% (Murphy 2002). Table 3-5 summarizes estimated *plant available water* values adjusted for organic content for the four soil groups at Meadowbrook. *Plant available water* is expressed in both the VWC percent and also in inches per foot of soil depth.

Table 3-5 *Plant available water* adjusted for organic content (adapted from Murphy 2002).

Texture	Field Capacity (%)	Permanent Wilting Point (%)	Plant Available Water (%)	Plant Available Water (in/ft)
Sand	15	5	10	0.5
Loamy sand	19	5	12	1.0
Sandy loam	25	8	17	1.5
Silty clay loam	45	22	23	2.5

The concept of *carrying capacity* of the soil (the time required by the turf to deplete 50% of the *plant available water*) is introduced to relate *plant available water* with daily evapotranspiration rates using the following equation (Murphy 2002):

$$carrying\ capacity\ (days) = \frac{available\ water\ \left(\frac{in}{ft}\right) \times rooting\ depth\ (ft)}{evapotranspiration\ \left(\frac{in}{day}\right)} \quad (3\text{-}1)$$

Table 3-6 is constructed from the above equation to provide the *carrying capacity* of the four soil groups and corresponding rooting depths (measured during soil analysis, Section 2.3) at Meadowbrook along with typical evapotranspiration rates for north central Texas in the month of October (TexasET 2017). The next phase of this research will aim to develop time-based spatially-distributed irrigation maps from *PrISMM* θ_{rs} maps, weather forecasts and retrieved estimates of evapotranspiration.

As mentioned in Section 3.1., the *PrISMM* model accurately detects thresholds for $\theta_{rs} \leq 0.17$. These pixels are flagged and scheduled for irrigation using the full time interval for each day until the values return to within 20% of *field capacity*. The *PrISMM* model similarly flags pixels for $\theta_{rs} \geq 0.50$ which are removed from irrigation scheduling until the values return to within 20% of the *field capacity*. For values within 20% of field capacity, or, approximately a VWC of 17 – 54% depending on soil type, values are converted to percent *plant available water* in accordance with the

corresponding soil texture. The daily evapotranspiration rate (TexasET Network) and rooting depth (appx. 2.6 in) are used to determine the *carrying capacity*, i.e., the number of days for the *plant available water* to become 50% depleted. Irrigation is then scheduled in a manner as to restore *plant available water* (in/ft) to a level that will guarantee that *plant available water* shall remain at or above 50% until the next irrigation and/or rainfall event.

Table 3-6 Carrying capacity of soils for various evapotranspiration rates and rooting depths[1].

Soil Type	Evapotranspiration	Effective rooting depth (in)			
		2.0	3.0	4.0	5.0
	inches/day	*Time (days) to deplete 50% of available water*			
Sand	0.05	1.7	2.5	3.3	4.2
	0.10	0.8	1.3	1.7	2.1
	0.15	0.6	0.8	1.1	1.4
Loamy sand	0.05	3.3	5.0	6.7	8.3
	0.10	1.7	2.5	3.3	4.2
	0.15	1.1	1.7	2.2	2.8
Sandy loam	0.05	5.0	7.5	10.0	12.5
	0.10	2.5	3.8	5.0	6.3
	0.15	1.7	2.5	3.3	4.2
Silty clay loam	0.05	8.3	12.5	16.7	20.8
	0.10	4.2	6.3	8.3	10.4
	0.15	2.8	4.2	5.6	6.9

[1] Based on depletion of 50% of the available water.

In the case of Meadowbrook, the *PrISMM* maps helped to identify areas that were chronically dry, including long stretches of fairway (Figure A-1 through Figure A-6) where compaction is intensified by frequent golf cart and foot traffic, causing more runoff to be generated and moisture to be rapidly lost. In order to improve infiltration in the well-irrigated, though chronically dry zones, the precipitation rate of the sprinkler heads should be reduced to promote infiltration. The duration may also be reduced while performing a second or third irrigation event later the same night. Chronically wet areas consisted of topographic lows where runoff was temporarily stored as ponded water. This is indicative of excessive precipitation rates within the

surrounding area. Precipitation rates should subsequently be reduced while simultaneously increasing the duration so that the precipitation depth remains the same. Also of note, the putting greens –*which have a high infiltration rate*– must be irrigated nearly every day in the spring, summer and fall in the absence of sufficient rainfall. This results in chronic wet spots on the edges of the greens where the sandy soil rapidly transitions to loamy sand. This could be addressed by installing plastic liners under the putting greens to prevent excessive infiltration and thus reduce the amount of irrigation water required.

Chapter 4 Conclusion

4.1. Conclusion and Future Work

This study presented the application of a novel remote sensing system known as *Precision Irrigation Soil Moisture Mapper* (PrISMM) for deriving soil moisture estimates to determine watering requirements for urban landscapes. *PrISMM* was implemented at a golf course in Arlington, Texas to demonstrate the feasibility of precision irrigation based on spatially-distributed VWC estimates as the primary decision variable. High-resolution, multispectral imagery acquired using an unmanned aerial vehicle (UAV), combined with site-specific soil analysis and surface energy balance modeling serve as the main components for a thermal inertia approach to the estimation of volumetric water content (VWC). Diurnal temperature variations, measured with a thermal camera, are related to ground heat flux to derive the thermal inertia estimates. Remotely-sensed estimates of thermal inertia were then used for VWC retrieval based on actual soil physical parameters with a resolution of 8.6 cm.

The accuracy of *PrISMM* was quantified using ground truthing data from a time domain reflectometry (TDR) soil moisture sensor. Goodness-of-fit statistics of actual *versus* predicted VWC indicate good model accuracy: (r: 0.89, R^2: 0.79, RMSE: 0.04, MAE: 0.03). It was further discussed how *PrISMM* data may be combined with daily evapotranspiration rates and weather forecasts to determine the duration and frequency of irrigation requirements based on irrigation management zones. Advantages of using the *PrISMM* model over traditional methods for irrigation water management decisions include:

- Timely and accurate, spatially-distributed soil moisture estimates;
- A wide range of operating conditions with easy and flexible use;

- A model with a clear physical meaning;
- The identification of deficiencies in irrigation systems by detecting chronic wet and dry spots;
- Provision of continuous, high resolution estimates which are simply impossible to obtain using *in situ* sensors;
- Excellent density and continuity of data, covering ~0.1 km^2 in 30 minutes (compared to 1.5 hours for 100 TDR readings;
- The allowance of operation of independent sprinkler heads with specified durations and frequencies.

One weakness of the model is that the current methodology cannot take into account heterogeneity or thermographic anomalies in subsoils. These regions may cause non-uniform heating. It is also currently unknown how *PrISMM* will perform in cloudy or overcast conditions. Because the surface energy balance model assumes a cloudless sky, a four-component net radiometer will be installed on site to evaluate the model performance in a wider range of atmospheric conditions. Also unclear is how *PrISMM* will perform during winter months when days are shorter and the effective root zone is deeper. In particular, it is unclear how the system will be impacted by frost and the dormancy of grass. The next phase of this research will aim to resolve these issues as well as develop time-based spatially-distributed irrigation maps from *PrISMM* θ_{rs} maps, weather forecasts and evapotranspiration rates. For the present, however, all findings indicate that *PrISMM* offers superior spatial and temporal resolution compared to *in situ* methods and may be implemented to precisely irrigate urban landscapes, thus saving millions of gallons of water annually.

APPENDIX A

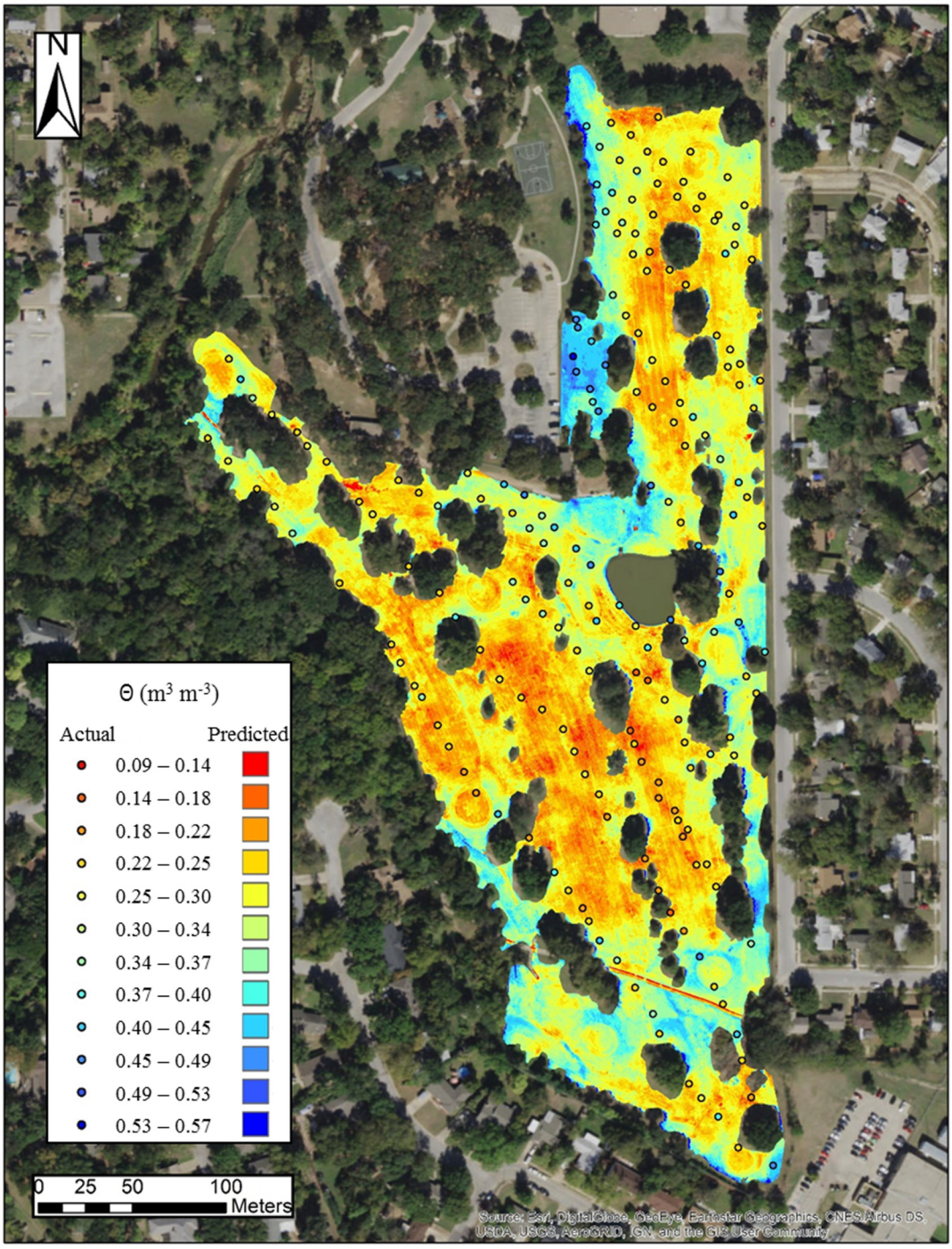

Figure A-1 *PrISMM* soil moisture map (Volumetric Water Content (m^3 m^{-3})) *versus* Time Domain Reflectometry measurements: October 12, 2017.

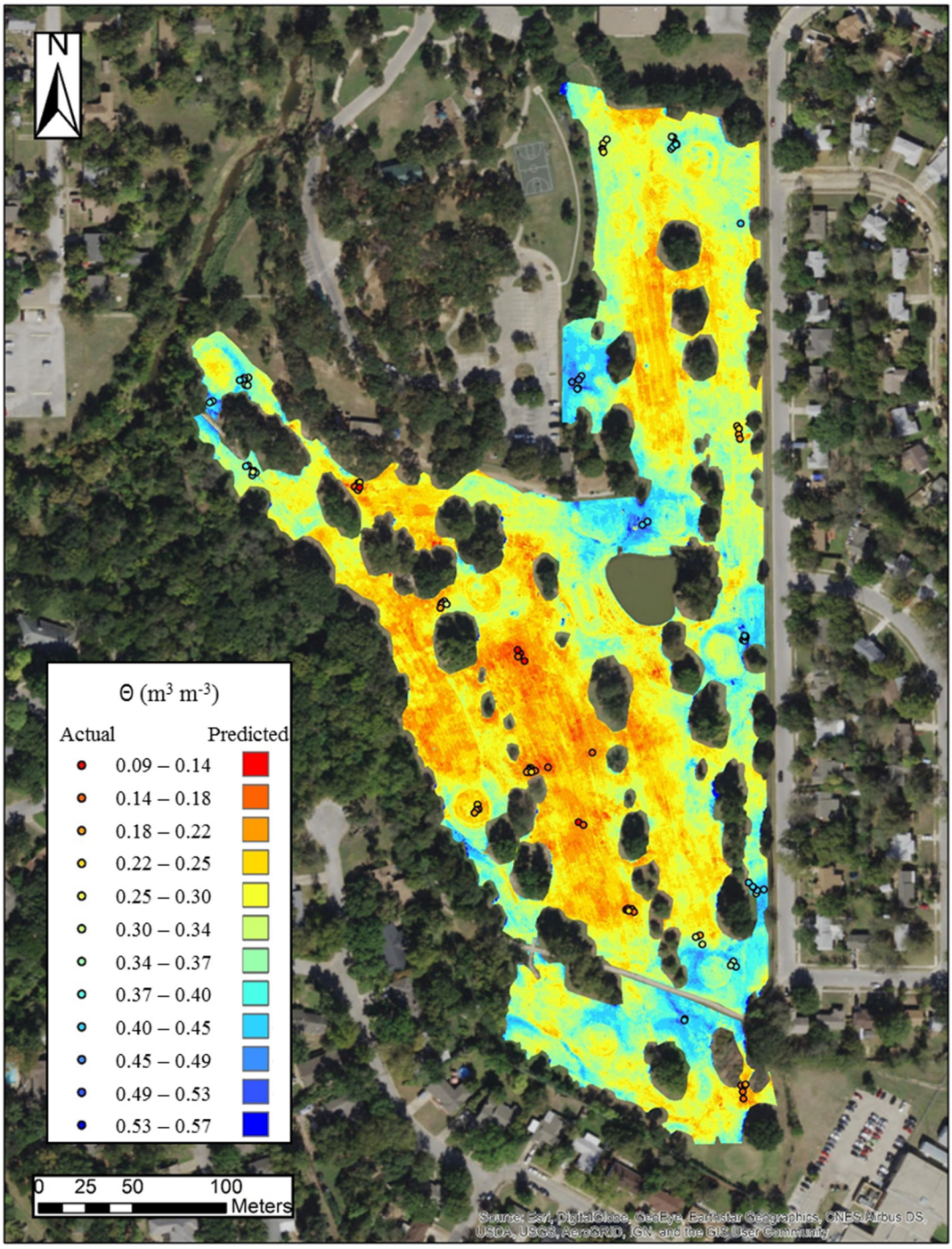

Figure A-2 *PrISMM* soil moisture map (Volumetric Water Content (m^3 m^{-3})) *versus* Time Domain Reflectometry measurements: October 17, 2017.

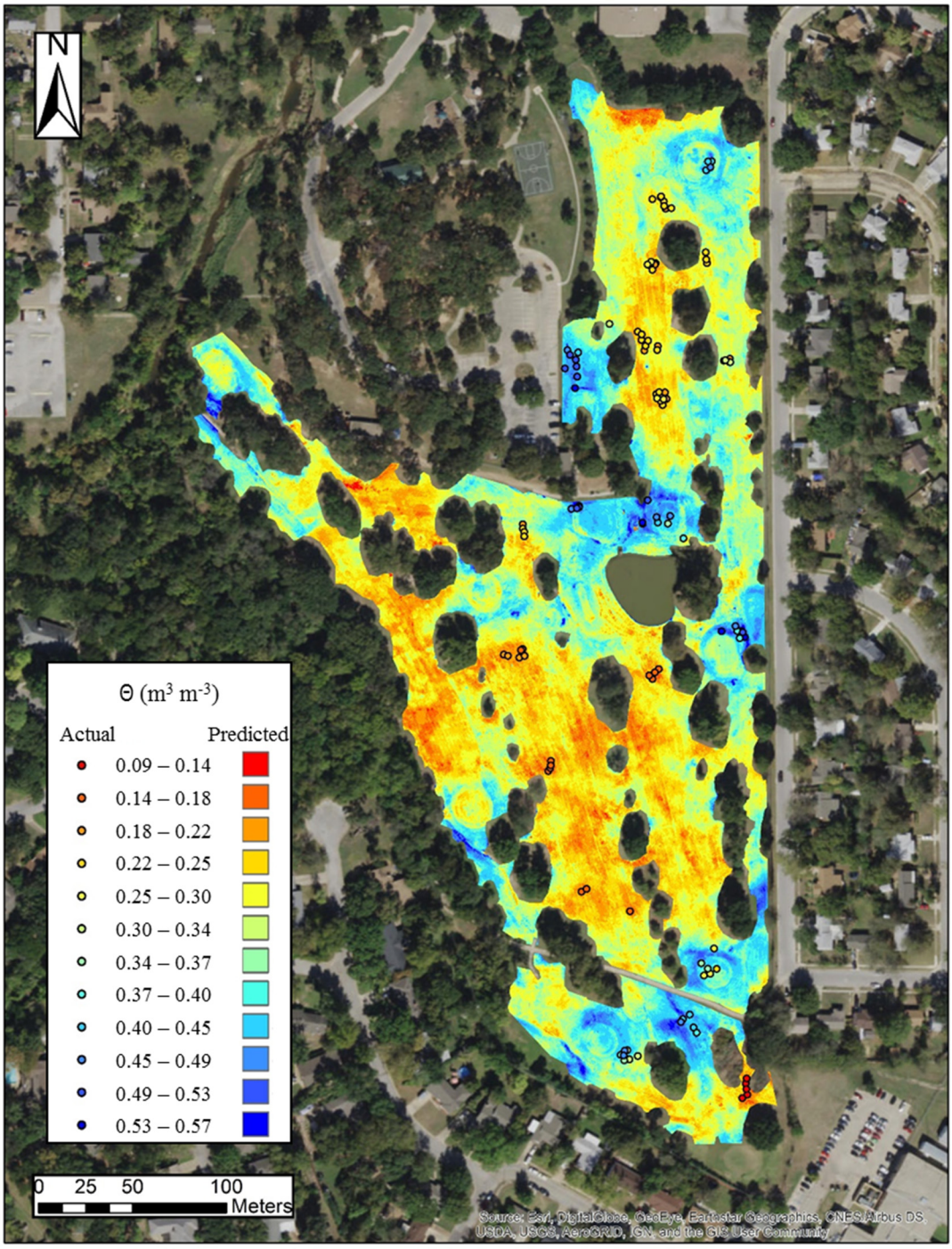

Figure A-3 *PrISMM* soil moisture map (Volumetric Water Content (m^3 m^{-3})) *versus* Time Domain Reflectometry measurements: October 18, 2017.

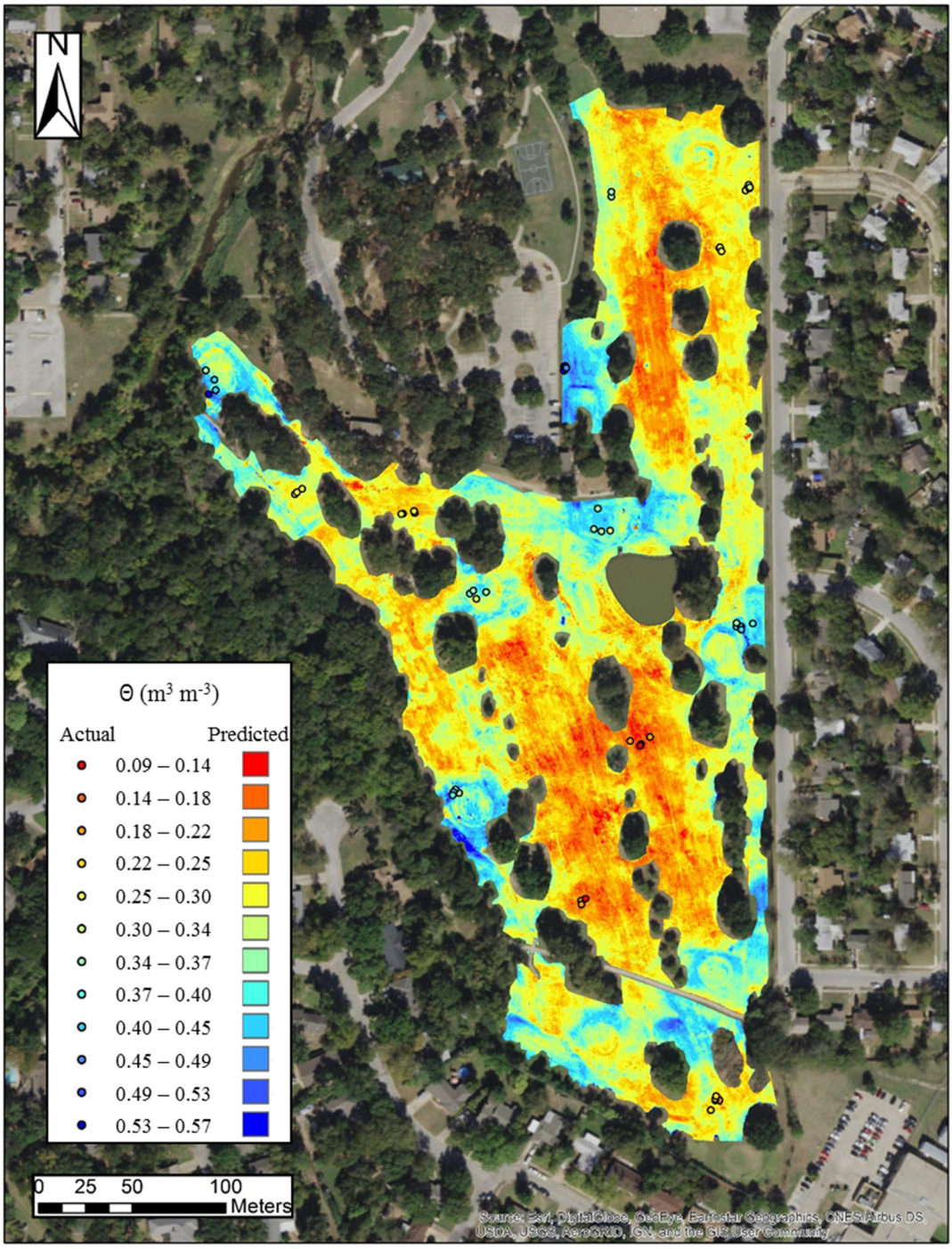

Figure A-4 *PrISMM* soil moisture map (Volumetric Water Content (m^3 m^{-3})) *versus* Time Domain Reflectometry measurements: October 25, 2017.

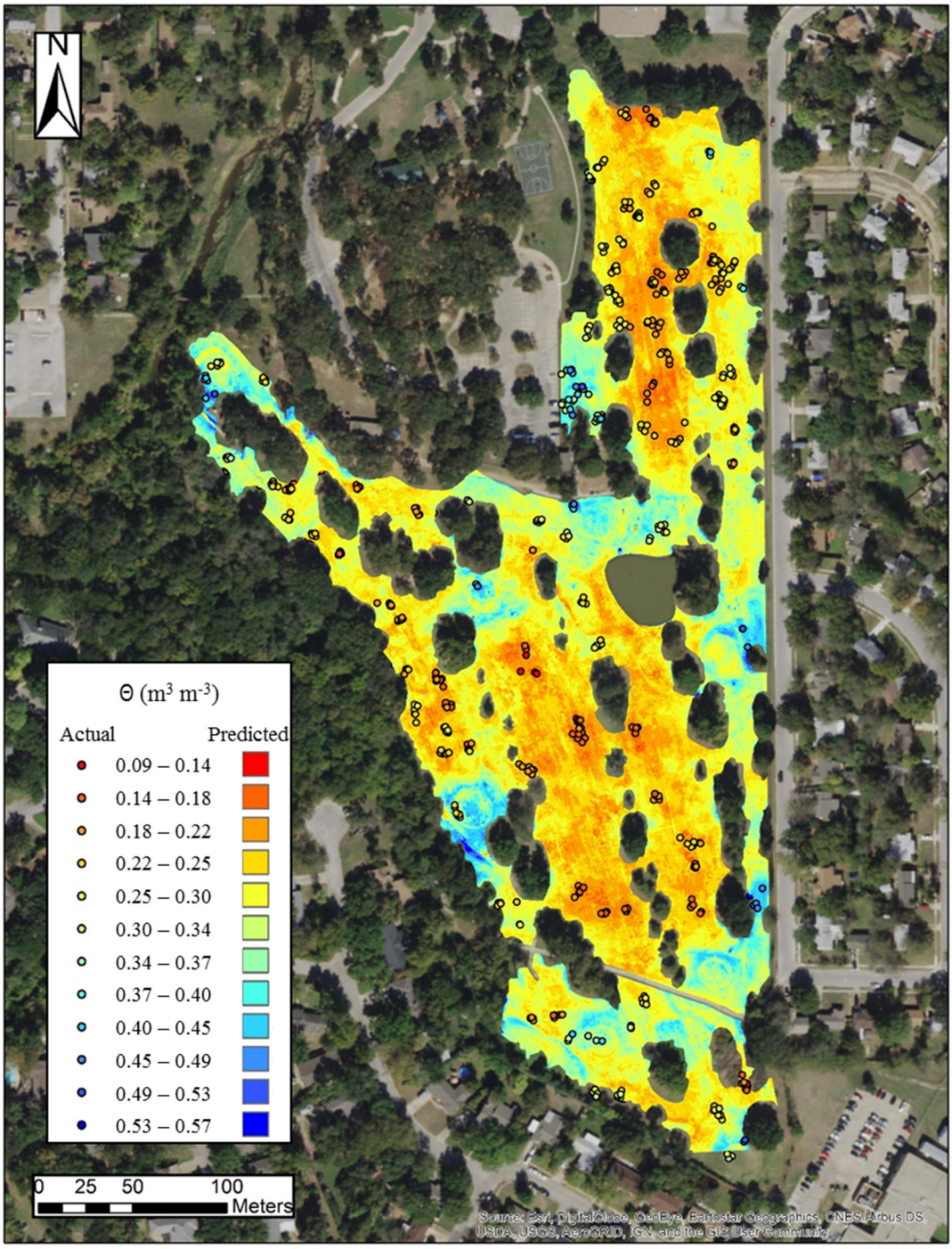

Figure A-5 *PrISMM* soil moisture map (Volumetric Water Content (m^3 m^{-3})) *versus* Time Domain Reflectometry measurements: October 29, 2017.

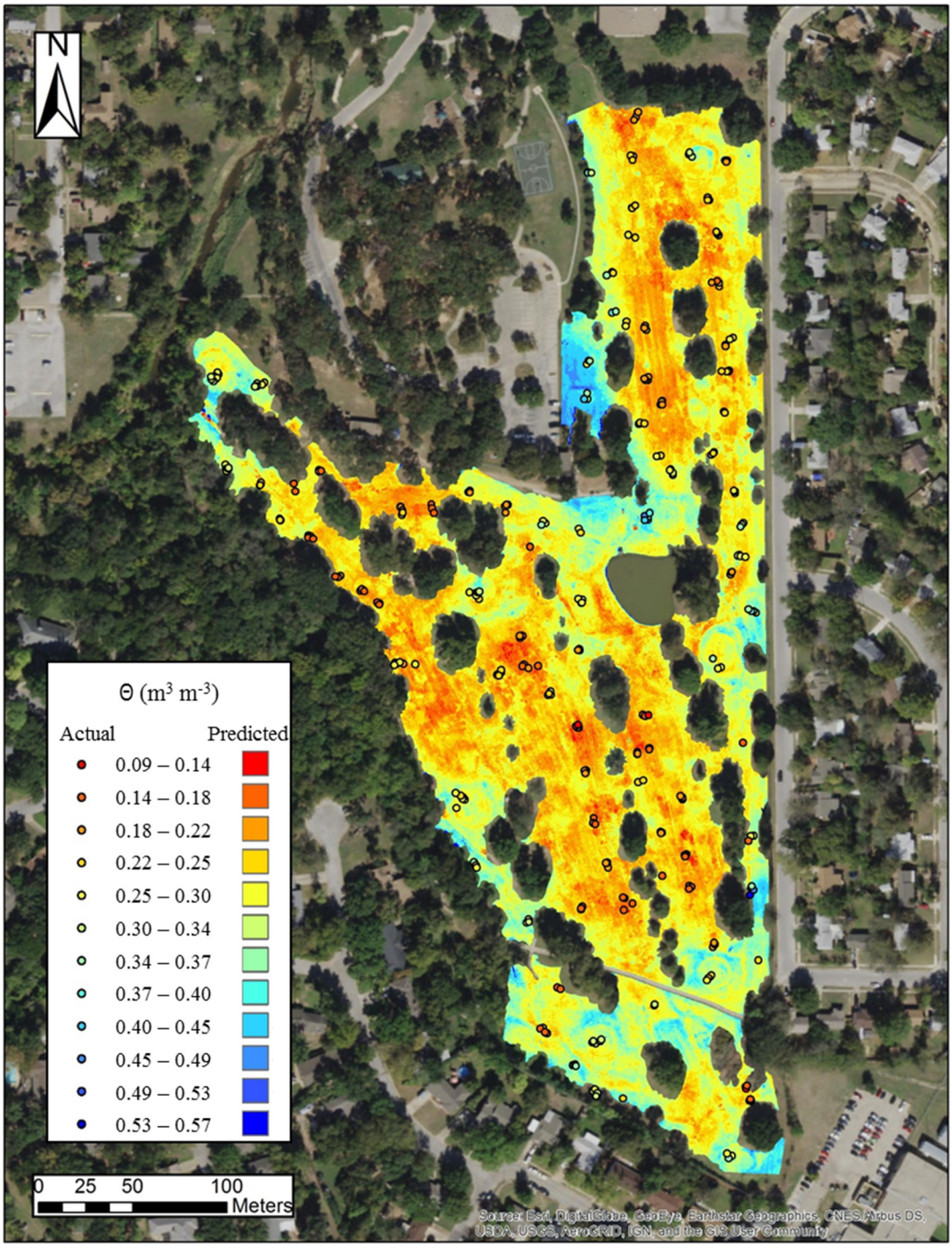

Figure A-6 *PrISMM* soil moisture map (Volumetric Water Content (m^3 m^{-3})) *versus* Time Domain Reflectometry measurements: October 30, 2017.

a.

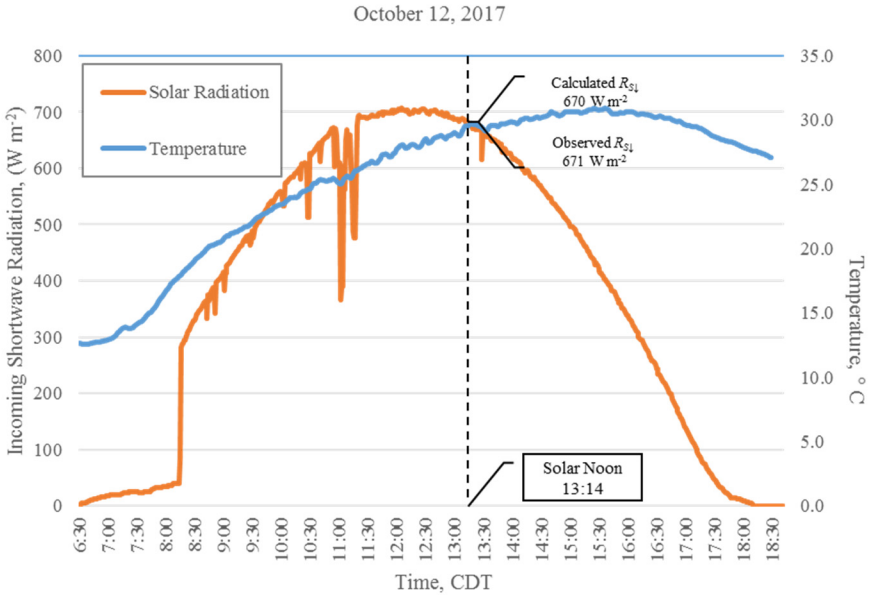
October 12, 2017
Solar Radiation
Temperature
Calculated $R_{S\downarrow}$ 670 W m^{-2}
Observed $R_{S\downarrow}$ 671 W m^{-2}
Solar Noon 13:14
Incoming Shortwave Radiation, (W m^{-2})
Temperature, ° C
Time, CDT

b.

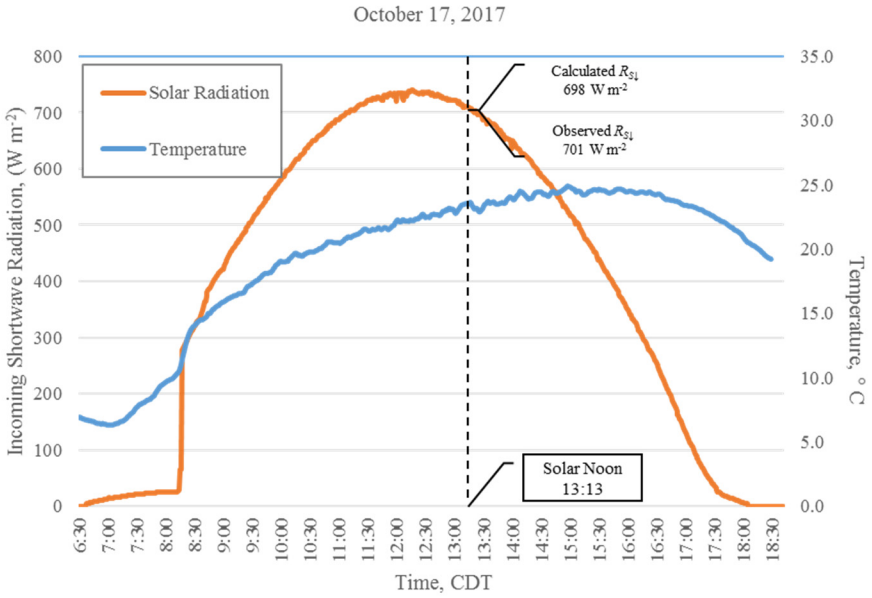
October 17, 2017
Solar Radiation
Temperature
Calculated $R_{S\downarrow}$ 698 W m^{-2}
Observed $R_{S\downarrow}$ 701 W m^{-2}
Solar Noon 13:13
Incoming Shortwave Radiation, (W m^{-2})
Temperature, ° C
Time, CDT

c.

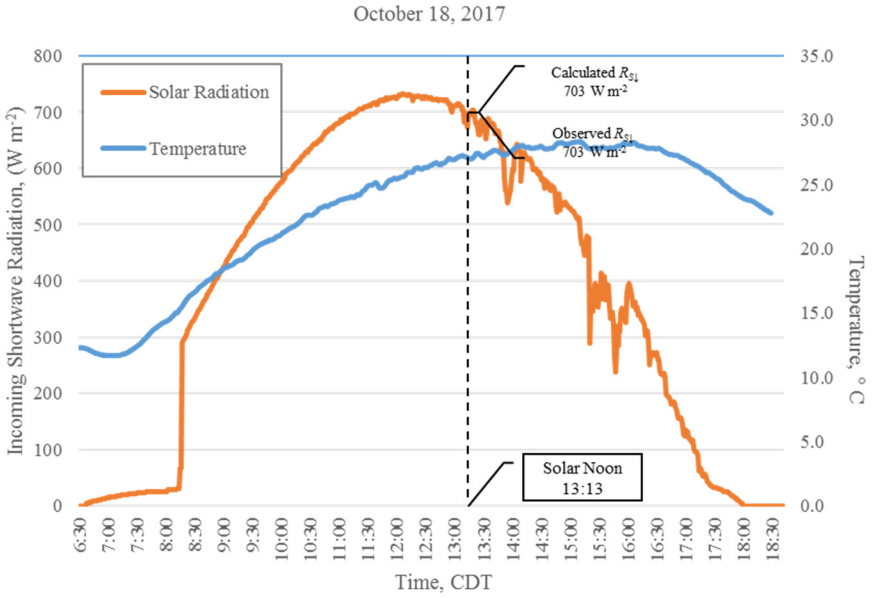
October 18, 2017
Solar Radiation
Temperature
Calculated $R_{S\downarrow}$ 703 W m^{-2}
Observed $R_{S\downarrow}$ 703 W m^{-2}
Solar Noon 13:13
Incoming Shortwave Radiation, (W m^{-2})
Temperature, ° C
Time, CDT

d.

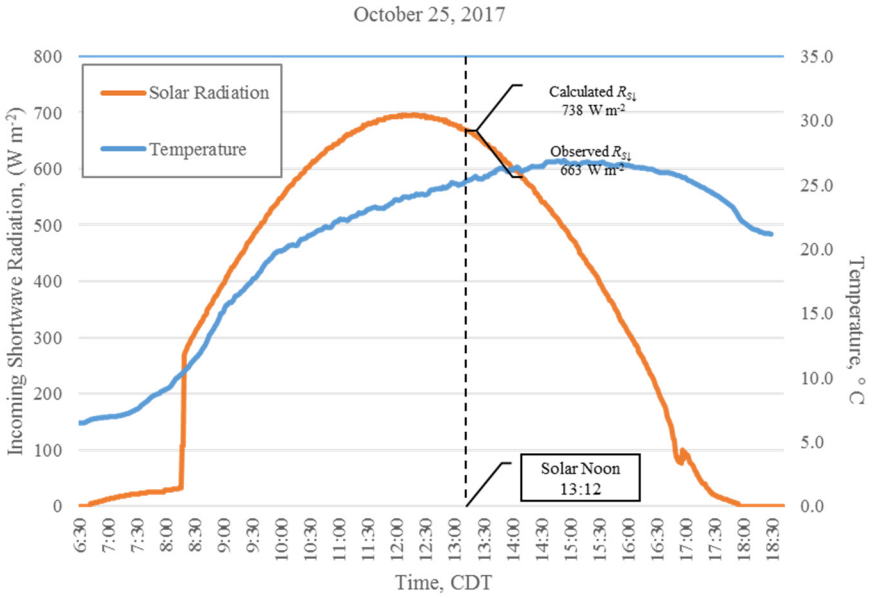
October 25, 2017
Solar Radiation
Temperature
Calculated $R_{S\downarrow}$ 738 W m^{-2}
Observed $R_{S\downarrow}$ 663 W m^{-2}
Solar Noon 13:12
Incoming Shortwave Radiation, (W m^{-2})
Temperature, ° C
Time, CDT

e.

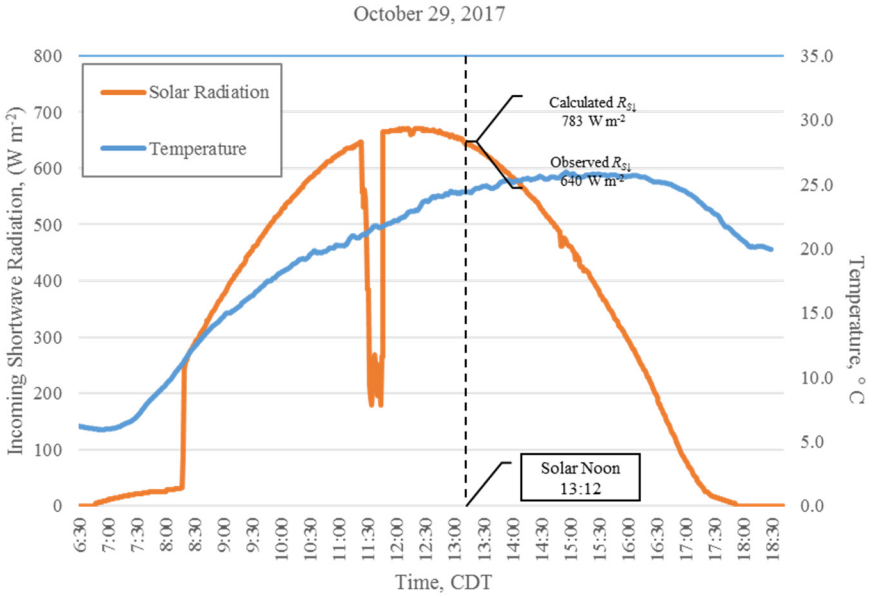

f.

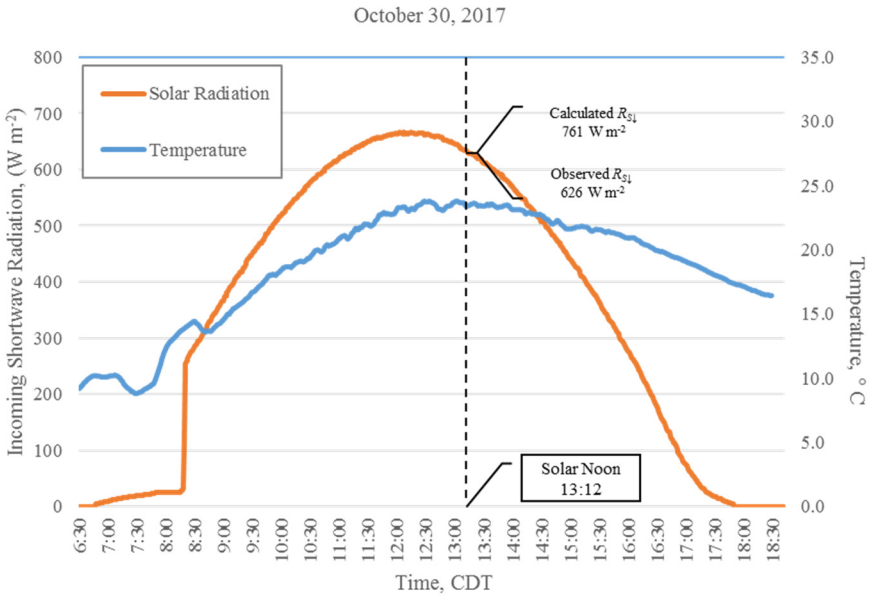

Figure A-7 Incoming solar radiation (calculated *versus* observed) at solar noon: (a) October 12; (b) October 17; (c) October 18; (d) October 25; (e) October 29; (f) October 30, 2017.

a.

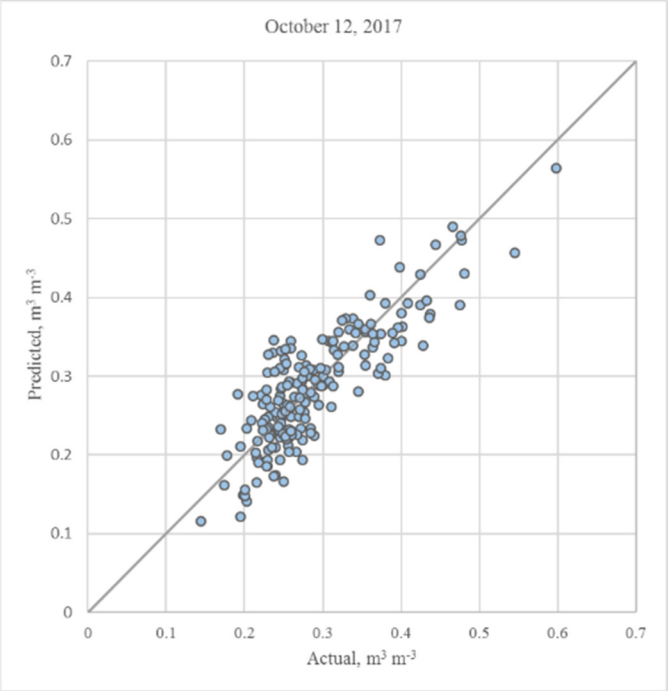
October 12, 2017
Predicted, m³ m⁻³
Actual, m³ m⁻³
0
0.1
0.2
0.3
0.4
0.5
0.6
0.7

b.

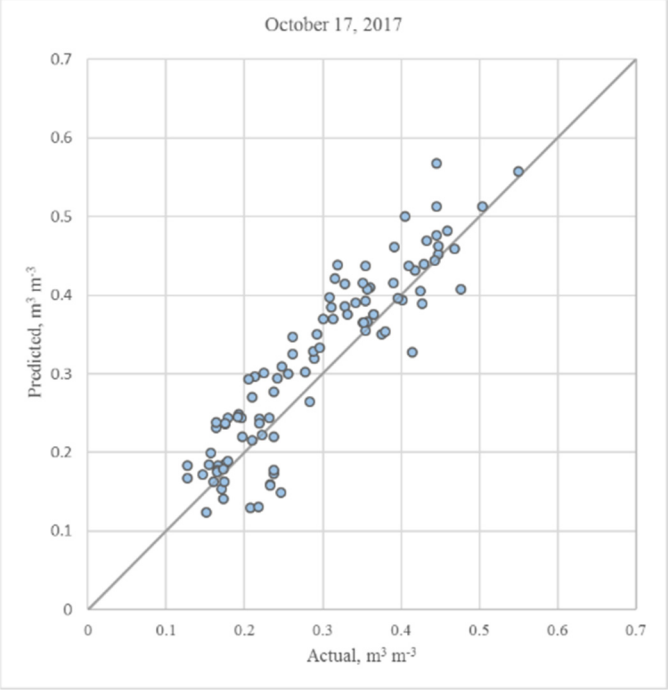
October 17, 2017
Predicted, m³ m⁻³
Actual, m³ m⁻³
0
0.1
0.2
0.3
0.4
0.5
0.6
0.7

c.

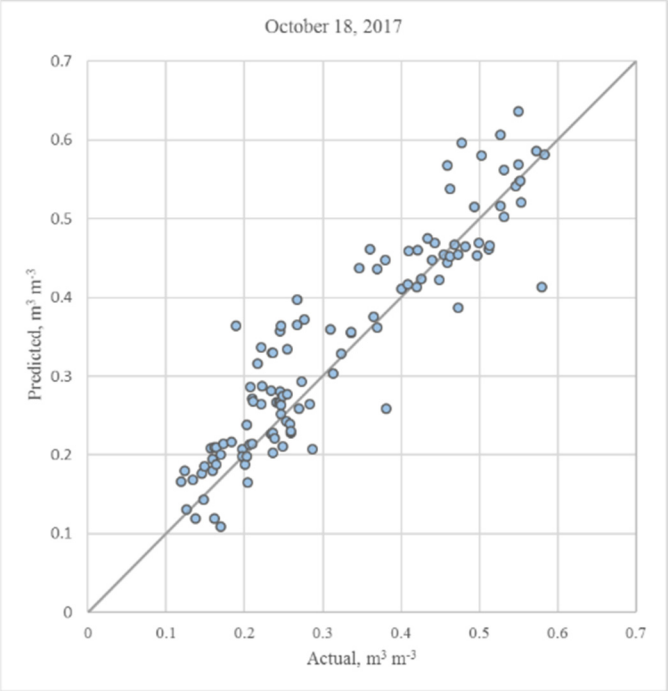
October 18, 2017
Predicted, m³ m⁻³
Actual, m³ m⁻³
0
0.1
0.2
0.3
0.4
0.5
0.6
0.7

d.

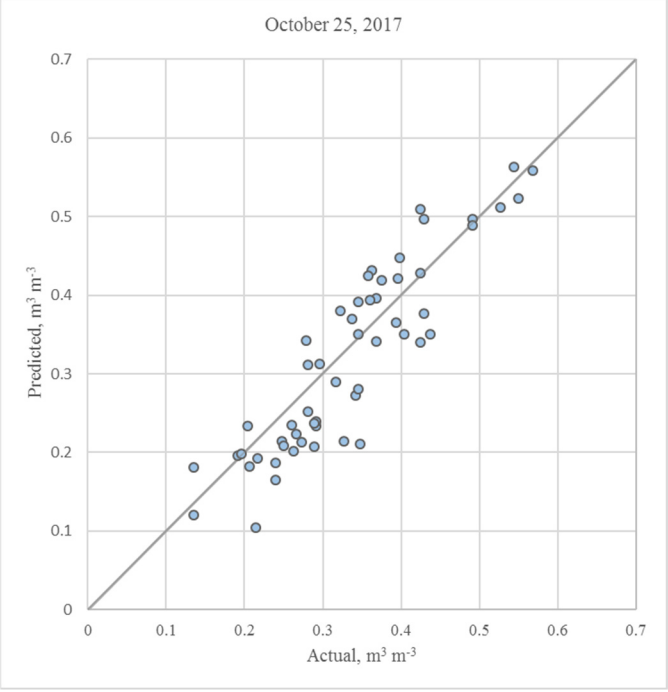
October 25, 2017
Predicted, m³ m⁻³
Actual, m³ m⁻³
0
0.1
0.2
0.3
0.4
0.5
0.6
0.7

e.

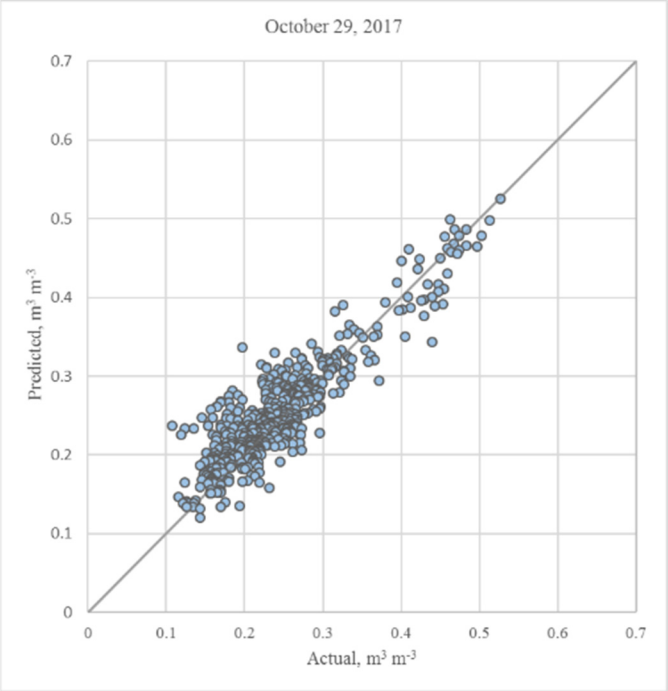

f.

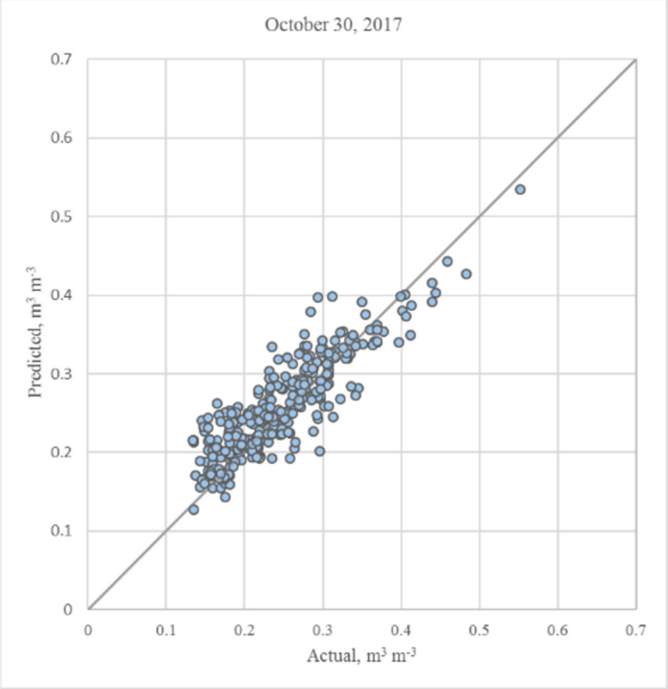

Figure A-8 Scatter plots of actual vs. predicted Volumetric Water Content ($m^3\ m^{-3}$): (a) October 12; (b) October 17; (c) October 18; (d) October 25; (e) October 29; (f) October 30, 2017.

a.

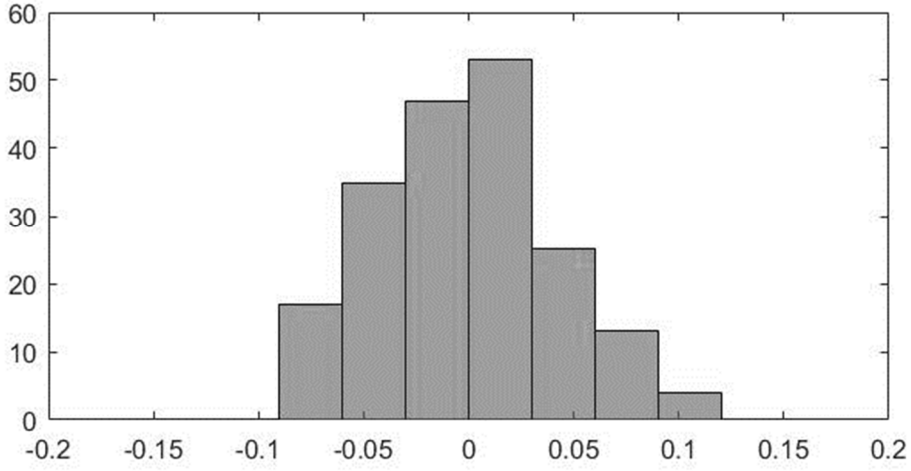
60
50
40
30
20
10
0
-0.2
-0.15
-0.1
-0.05
0
0.05
0.1
0.15
0.2

b
.

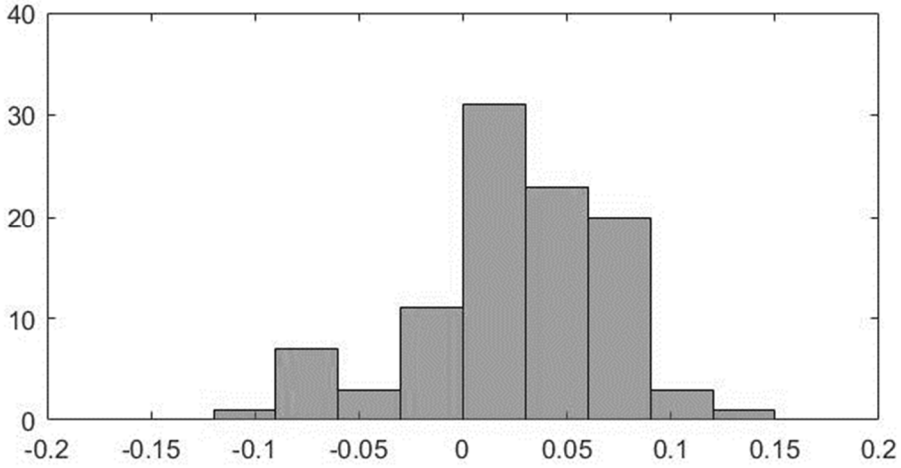
40
30
20
10
0
-0.2
-0.15
-0.1
-0.05
0
0.05
0.1
0.15
0.2

c.

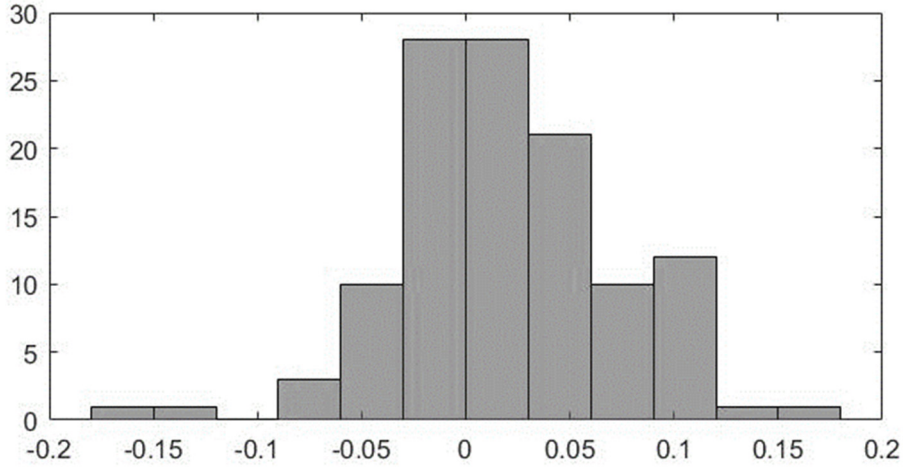
30
25
20
15
10
5
0
-0.2
-0.15
-0.1
-0.05
0
0.05
0.1
0.15
0.2

d
.

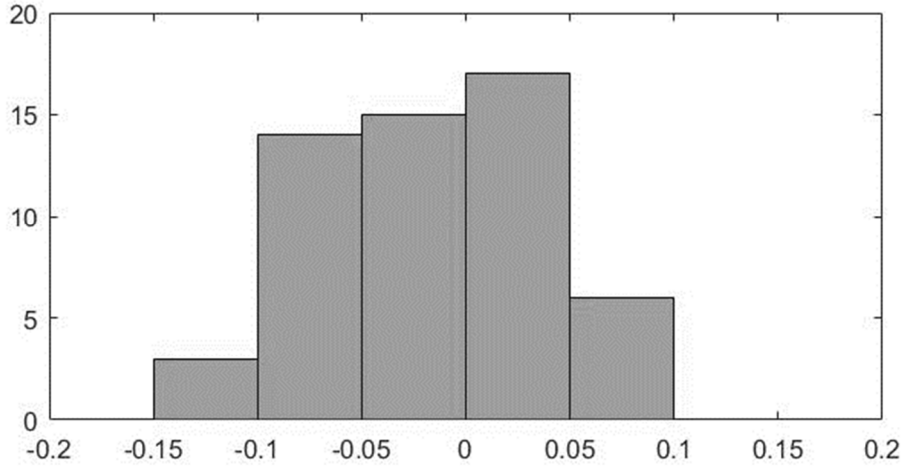
20
15
10
5
0
-0.2
-0.15
-0.1
-0.05
0
0.05
0.1
0.15
0.2

e.

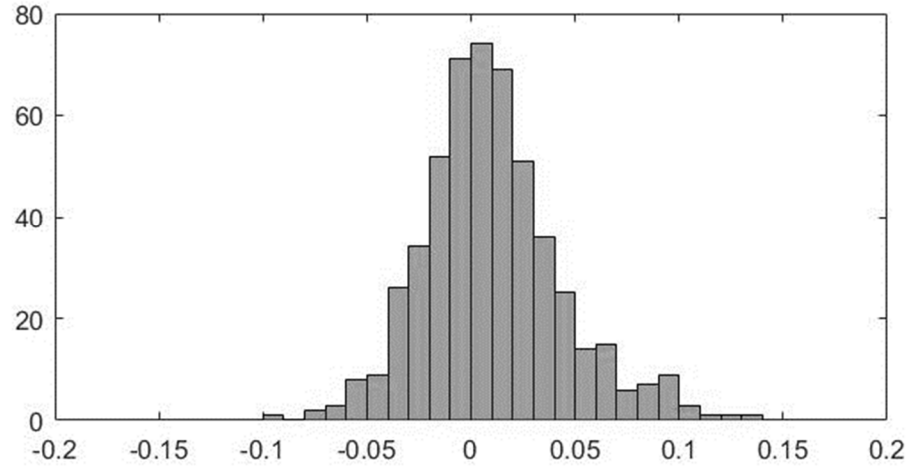

f.

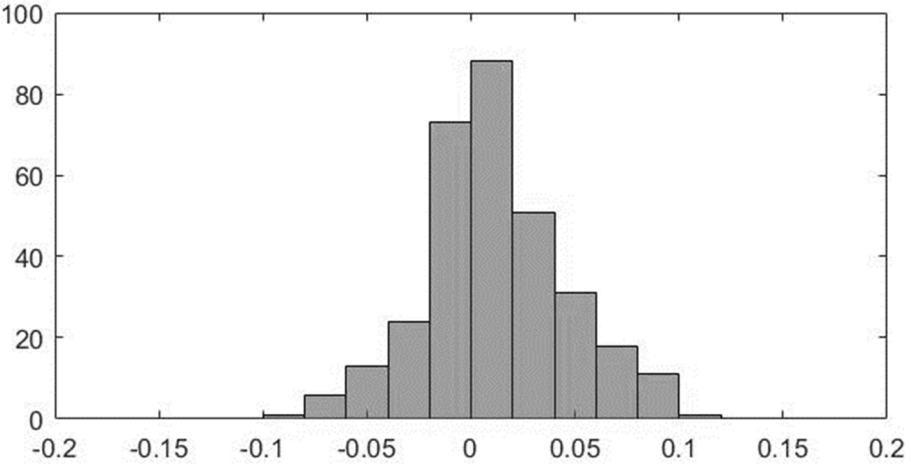

Figure A-9 Histograms of actual vs. predicted Volumetric Water Content (m^3 m^{-3}): (a) October 12; (b) October 17; (c) October 18; (d) October 25; (e) October 29; (f) October 30, 2017.

a.

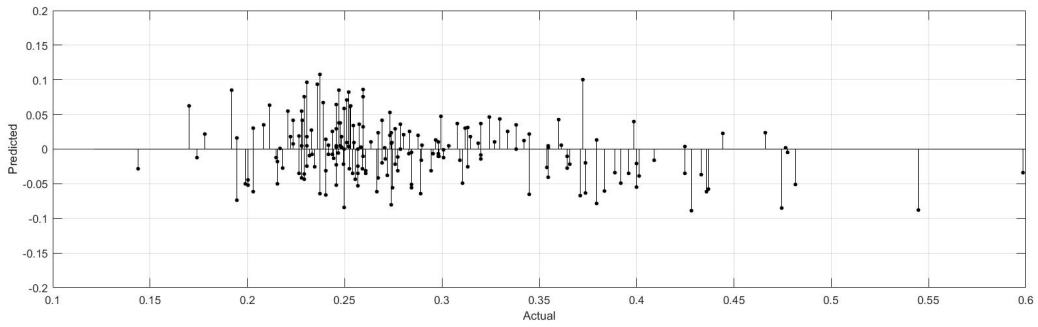
Predicted
Actual
0.2
0.15
0.1
0.05
0
-0.05
-0.1
-0.15
-0.2
0.1
0.15
0.2
0.25
0.3
0.35
0.4
0.45
0.5
0.55
0.6

b.

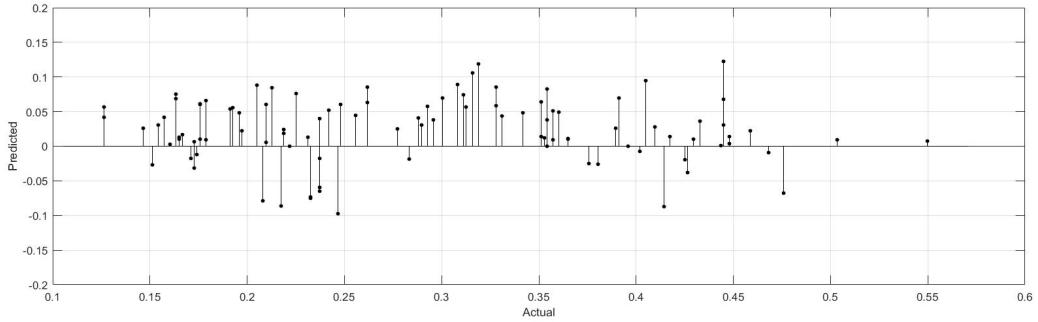
Predicted
Actual
0.2
0.15
0.1
0.05
0
-0.05
-0.1
-0.15
-0.2
0.1
0.15
0.2
0.25
0.3
0.35
0.4
0.45
0.5
0.55
0.6

c.

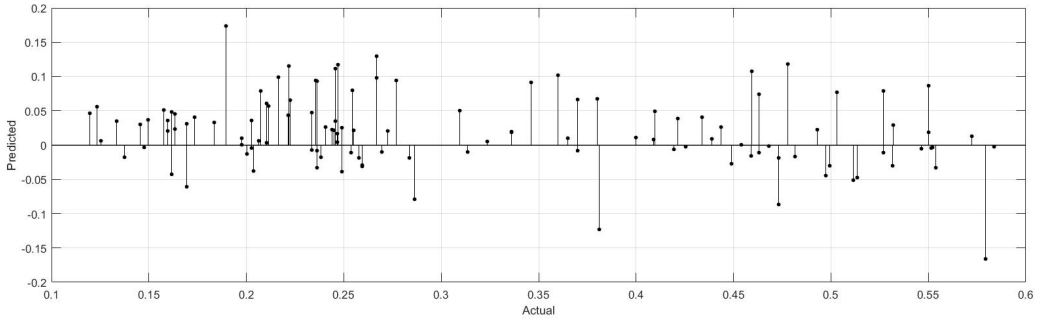
Predicted
Actual
0.2
0.15
0.1
0.05
0
-0.05
-0.1
-0.15
-0.2
0.1
0.15
0.2
0.25
0.3
0.35
0.4
0.45
0.5
0.55
0.6

d.

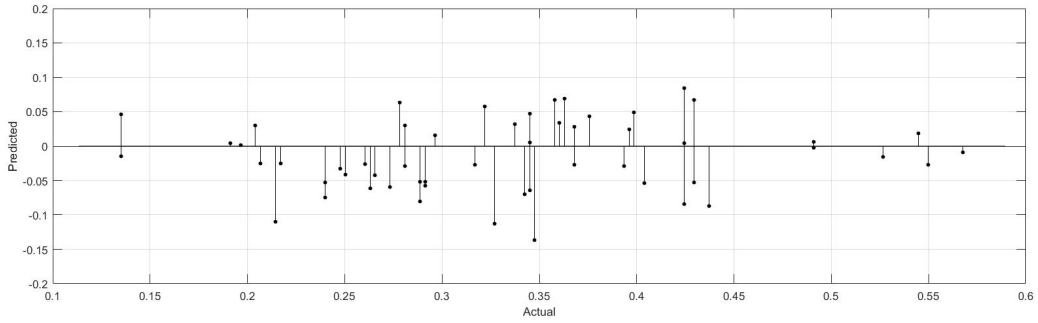

e.

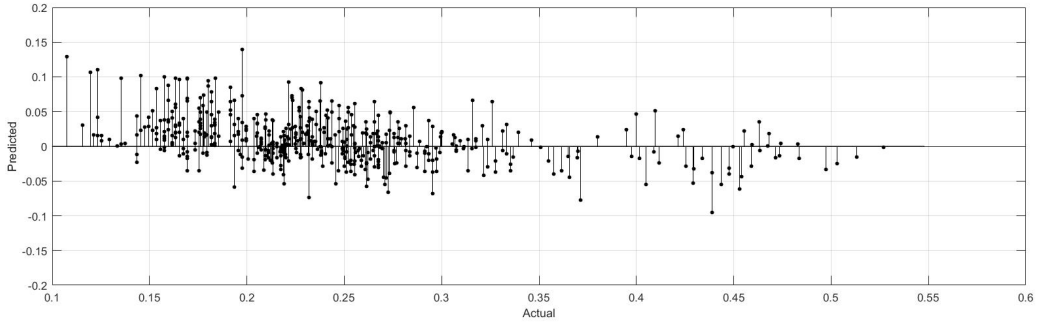

f.

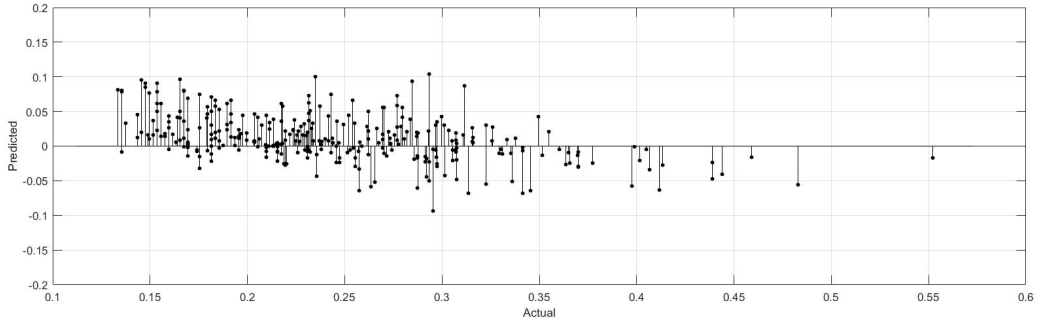

Figure A-10 *PrISMM* soil moisture map (Volumetric Water Content (m^3 m^{-3})) vs. Time Domain Reflectometry measurements: (a) October 12; (b) October 17; (c) October 18; (d) October 25; (e) October 29; (f) October 30, 2017.

REFERENCES

Achard, F., and D'Souza, G. (1994). Collection and pre-processing of NOAA-AVHRR 1 km resolution data for tropical forest resource assessment. Collection and pre-processing of NOAA-AVHRR 1 km resolution data for tropical forest resource assessment, rep., European Commission, Luxembourg.

Agüera-Vega, F., Carvajal-Ramírez, F., and Martínez-Carricondo, P. (2017). "Accuracy of Digital Surface Models and Orthophotos Derived from Unmanned Aerial Vehicle Photogrammetry." Journal of Surveying Engineering, 143(2), 04016025.

Akbar, R., Das, N., Entekhabi, D., and Moghaddam, M. (2016). "Active and Passive Microwave Remote Sensing Synergy for Soil Moisture Estimation." Satellite Soil Moisture Retrieval, 187–207.

Allen, R. G., Tasumi, M., and Trezza, R. (2007). "Satellite-Based Energy Balance for Mapping Evapotranspiration with Internalized Calibration (METRIC)—Model." Journal of Irrigation and Drainage Engineering, 133(4), 380–394.

Al-Yaari, A., Wigneron, J.-P., Ducharne, A., Kerr, Y., Wagner, W., Lannoy, G. D., Reichle, R., Bitar, A. A., Dorigo, W., Richaume, P., and Mialon, A. (2014). "Global-scale comparison of passive (SMOS) and active (ASCAT) satellite based microwave soil moisture retrievals with soil moisture simulations (MERRA-Land)." Remote Sensing of Environment, 152, 614–626.

Ångström, A. (1925). "The Albedo of Various Surfaces of Ground." Geografiska Annaler, 7, 323.

ASTM. (2007). "Standard test method for density and unit weight of soil in place by sand-cone method", essay, ASTM International, Philadelphia, PA.

Bach, H., and Mauser, W. (1994). "Modelling and model verification of the spectral reflectance of soils under varying moisture conditions." Proceedings of IGARSS 94 - 1994 IEEE International Geoscience and Remote Sensing Symposium.

Baghdadi, N., Camus, P., Beaugendre, N., Issa, O. M., Zribi, M., Desprats, J. F., Rajot, J. L., Abdallah, C., and Sannier, C. (2011). “Estimating Surface Soil Moisture from TerraSAR-X Data over Two Small Catchments in the Sahelian Part of Western Niger.” Remote Sensing, 3(6), 1266–1283.

Bastiaanssen, W., Menenti, M., Feddes, R., and Holtslag, A. (1998). “A remote sensing surface energy balance algorithm for land (SEBAL). 1. Formulation.” Journal of Hydrology, 212-213, 198–212.

Bastiaanssen, W. (2000). “SEBAL-based sensible and latent heat fluxes in the irrigated Gediz Basin, Turkey.” Journal of Hydrology, 229(1-2), 87–100.

Berni, J., Zarco-Tejada, P., Suarez, L., and Fereres, E. (2009). “Thermal and Narrowband Multispectral Remote Sensing for Vegetation Monitoring From an Unmanned Aerial Vehicle.” IEEE Transactions on Geoscience and Remote Sensing, 47(3), 722–738.

Bogena, H., Huisman, J., Oberdörster, C., and Vereecken, H. (2007). “Evaluation of a low-cost soil water content sensor for wireless network applications.” Journal of Hydrology, 344(1-2), 32–42.

Boland, J. J. (1997). “Assessing Urban Water Use and the Role of Water Conservation Measures Under Climate Uncertainty.” Climate Change and Water Resources Planning Criteria, 157–176.

Bowers, S. A., and Smith, S. J. (1972). “Spectrophotometric determination of soil water content.” Environmental Sciences and Pollution Management, 36(6), 978–980.

Brevik, E. C., and Batten, R. A. (2012). “Evaluation of the FieldScout TDR300 for Determining Volumetric Water Content in Sandy South Georgia Soils.” Soil Horizons, 53(6), 27.

Brookes, J. D., Ainger, C. M., Howe, C., Norton, J. W., and Schladow, G. (2010). “Water and climate change: challenges for the 21st century.” Journal of Water and Climate Change, 1(1).

Brooks, F. A. (1952). “Atmospheric Radiation And Its Reflection From The Ground.” Journal of Meteorology, 9(1), 41–52.

Cabrera, R. I., Wagner, K. L., and Wherley, B. (2013). “An Evaluation of Urban Landscape Water Use in Texas.” Texas Water Journal, 4(2), 14–27.

Campbell, G. S., and Norman, J. M. (1998). Introduction to environmental biophysics. Springer, New York.

Carlson, T. N., Dodd, J. K., Benjamin, S. G., and Cooper, J. N. (1981). “Satellite Estimation of the Surface Energy Balance, Moisture Availability and Thermal Inertia.” Journal of Applied Meteorology, 20(1), 67–87.

Carlson, T. N. (1986). “Regional-scale estimates of surface moisture availability and thermal inertia using remote thermal measurements.” Remote Sensing Reviews, 1(2), 197–247.

Carslaw, H. S., and Jaeger, J. C. (1959). Conduction of Heat in Solids. Oxford University Press, London, UK.

Cho, E., Choi, M., and Wagner, W. (2015a). “An assessment of remotely-sensed surface and root zone soil moisture through active and passive sensors in northeast Asia.” Remote Sensing of Environment, 160, 166–179.

Cho, E., Vasconcelos, G. A., and Choi, M. (2015b). “Validation Study of Active Microwave Soil Moisture Products in Korea and Brazil.” International Journal of Engineering and Technology, 7(3), 219–222.

Choudhury, B. J., Schmugge, T. J., Chang, A., and Newton, R. W. (1979). “Effect of surface roughness on the microwave emission from soils.” Journal of Geophysical Research, 84(C9), 5699.

Chow, V. T., Maidment, D. R., and Mays, L. W. (2013). Applied hydrology. McGraw-Hill Professional, New York.

Chung, G., Lansey, K., and Bayraksan, G. (2009). “Reliable water supply system design under uncertainty.” Environmental Modelling & Software, 24(4), 449–462.

Coppo, P., Ferrazzoli, P., Paloscia, S., Pampaloni, P., Schiavon, G., and Solimiui, D. (1990). “Sensitivity Of Active And Passive Microwave Sensors To Soil Moisture Of Vegetated Fields.” 10th Annual International Symposium on Geoscience and Remote Sensing.

Cuenca, R., Ciotti, S., and Hagimoto, Y. (2013). “Application of Landsat to Evaluate Effects of Irrigation Forbearance.” Remote Sensing, 5(8), 3776–3802.

Dalal, R. C., and Henry, R. J. (1986). “Simultaneous Determination of Moisture, Organic Carbon, and Total Nitrogen by Near Infrared Reflectance Spectrophotometry1.” Soil Science Society of America Journal, 50(1), 120.

de Vries, D.A. (1963). “Thermal properties of soils.” Physics of plant environment, 210–235.

Fabre, S., Briottet, X., and Lesaignoux, A. (2015). “Estimation of Soil Moisture Content from the Spectral Reflectance of Bare Soils in the 0.4–2.5 μm Domain.” Sensors, 15(2), 3262–3281.

Feng, Q., Liu, J., and Gong, J. (2015). “Urban Flood Mapping Based on Unmanned Aerial Vehicle Remote Sensing and Random Forest Classifier—A Case of Yuyao, China.” Water, 7(4), 1437–1455.

Fenstermaker-Shaulis, L. K., Leskys, A., and Devitt, D. A. (1997). “Utilization of Remotely Sensed Data to Map and Evaluate Turfgrass Stress Associated with Drought.” Journal of Turfgrass Management, 2(1), 65–81.

Ficklin, D. L., Stewart, I. T., and Maurer, E. P. (2012). “Effects of projected climate change on the hydrology in the Mono Lake Basin, California.” Climatic Change, 116(1), 111–131.

FLIR (2016). FLIR Vue Pro and Vue Pro R User Guide. 436-0013-10. Rev. 110. <http://www.flir.com/uploadedFiles/sUAS/Products/Vue-Pro/> (Jun. 21, 2017).

Gonzalez-Dugo, V., Goldhamer, D., Zarco-Tejada, P. J., and Fereres, E. (2014). “Improving the precision of irrigation in a pistachio farm using an unmanned airborne thermal system.” Irrigation Science, 33(1), 43–52.

Hardin, P., and Jackson, M. (2005). “An Unmanned Aerial Vehicle for Rangeland Photography.” Rangeland Ecology & Management, 58(4), 439–442.

Hassan-Esfahani, L., Torres-Rua, A., Jensen, A., and Mckee, M. (2015). “Assessment of Surface Soil Moisture Using High-Resolution Multi-Spectral Imagery and Artificial Neural Networks.” Remote Sensing, 7(3), 2627–2646.

Hassan-Esfahani, L., Torres-Rua, A., Jensen, A., and Mckee, M. (2017). “Spatial Root Zone Soil Water Content Estimation in Agricultural Lands Using Bayesian-Based Artificial Neural Networks and High- Resolution Visual, NIR, and Thermal Imagery.” Irrigation and Drainage, 66(2), 273–288.

Heathman, G. C., Starks, P. J., and Brown, M. A. (2003). “Time Domain Reflectometry Field Calibration in the Little Washita River Experimental Watershed.” Soil Science Society of America Journal, 67(1), 52.

Hingray, B. C. C., Picouet Cécile, Musy André, and Hingray, B. (2014). Hydrology: a science for engineers. CRC Press, Taylor & Francis Group, Boca Raton, FL.

Hoffmann, H., Nieto, H., Jensen, R., Guzinski, R., Zarco-Tejada, P., and Friborg, T. (2016). “Estimating evaporation with thermal UAV data and two-source energy balance models.” Hydrology and Earth System Sciences, 20(2), 697–713.

Hunt, E. R., Cavigelli, M., Daughtry, C. S. T., McMurtrey, J. E., and Walthall, C. L. (2005). “Evaluation of Digital Photography from Model Aircraft for Remote Sensing of Crop Biomass and Nitrogen Status.” Precision Agriculture, 6(4), 359–378.

Hunt, J. E. R., Hively, W. D., Fujikawa, S. J., Linden, D. S., Daughtry, C. S. T., and Mccarty, G. W. (2010). “Acquisition of NIR-Green-Blue Digital Photographs from Unmanned Aircraft for Crop Monitoring.” Remote Sensing, 2(1), 290–305.

Hutchinson, J. M. S. (2003). “Estimating Near Surface Soil Moisture Using Active Microwave Satellite Imagery And Optical Sensor Inputs.” Transactions of the ASAE, 46(2).

Idso, S. B., Jackson, R. D., and Reginato, R. J. (1976). “Compensating for Environmental Variability in the Thermal Inertia Approach to Remote Sensing of Soil Moisture.” Journal of Applied Meteorology, 15(8), 811–817.

Idso, S., Jackson, R., Pinter, P., Reginato, R., and Hatfield, J. (1981). “Normalizing the stress-degree-day parameter for environmental variability.” Agricultural Meteorology, 24, 45–55.

Jackson, R. D., Idso, S. B., and Reginato, R. J. (1976). “Calculation of evaporation rates during the transition from energy-limiting to soil-limiting phases using albedo data.” Water Resources Research, 12(1), 23–26.

Jackson, T. J. (1993). “III. Measuring surface soil moisture using passive microwave remote sensing.” Hydrological Processes, 7(2), 139–152.

Jacobsen, O., and Schjønning, P. (1993). “A laboratory calibration of time domain reflectometry for soil water measurement including effects of bulk density and texture.” Journal of Hydrology, 151(2-4), 147–157.

Jaeger, J. C. (1953). “Conduction of heat in a solid with periodic boundary conditions, with an application to the surface temperature of the moon.” Mathematical Proceedings of the Cambridge Philosophical Society, 49(02), 355.

Jenkins, D., and Vasigh, B. (2013). The Economic Impact of Unmanned Aircraft Systems Integration in the United States. The Economic Impact of Unmanned Aircraft Systems Integration in the United States, rep., AUVSI.

Jonard, F., Weiher Sadeghi, L., Schwank, M., Jadoon, K. Z., Vereecken, H., and Lambot, S. (2015). "Estimation of Hydraulic Properties of a Sandy Soil Using Ground-Based Active and Passive Microwave Remote Sensing." IEEE Transactions on Geoscience and Remote Sensing, 53(6), 3095–3109.

Kahle, A. B. (1976). "Thermal inertia imaging: A new geologic mapping tool". Geophysical research letters (0094-8276), 3(1), 26.

Kahle, A. B. (1977). "A simple thermal model of the Earths surface for geologic mapping by remote sensing." Journal of Geophysical Research, 82(11), 1673–1680.

Kanistras, K., Martins, G., Rutherford, M. J., and Valavanis, K. P. (2014). "Survey of Unmanned Aerial Vehicles (UAVs) for Traffic Monitoring." Handbook of Unmanned Aerial Vehicles, 2643–2666.

Kersten, M. S. (1949). Laboratory research for the determination of the thermal properties of soils: final report: June 1949. University of Minnesota, St. Paul, Min.

Kimes, D. S., Norman, J. M., and Walthall, C. L. (1985). "Modeling the Radiant Transfers of Sparse Vegetation Canopies." IEEE Transactions on Geoscience and Remote Sensing, GE-23(5), 695–704.

Kluitenberg, G. J., Das, B. S., and Bristow, K. L. (1995). "Error Analysis of Heat Pulse Method for Measuring Soil Heat Capacity, Diffusivity, and Conductivity." Soil Science Society of America Journal, 59(3), 719.

Klute, A., Gee, G. W., J. W. Bauder. (1986). "Particle-size Analysis." *SSSA Book Series: Methods of Soil Analysis: Part 1—Physical and Mineralogical Methods*. ASA, Madison, WI. p. 383-411.

Kojima, M. (1958). "On the relation between soil color and its moisture content." Soil and Plant Food, 3(4), 206.

Kustas, W. P., and Daughtry, C. S. (1990). “Estimation of the soil heat flux/net radiation ratio from spectral data.” Agricultural and Forest Meteorology, 49(3), 205–223.

Laliberte, A. S., and Rango, A. (2011). “Image Processing and Classification Procedures for Analysis of Sub-decimeter Imagery Acquired with an Unmanned Aircraft over Arid Rangelands.” GIScience & Remote Sensing, 48(1), 4–23.

Liang, S. (2004). Quantitative remote sensing of land surfaces. Wiley-Interscience, Hoboken (New Jersey).

Li, B., Ti, C., Zhao, Y., and Yan, X. (2016). “Estimating Soil Moisture with Landsat Data and Its Application in Extracting the Spatial Distribution of Winter Flooded Paddies.” Remote Sensing, 8(38).

Li, Z., Shi, J., and Guo, H. (2002). “Measuring soil moisture change with vegetation cover using passive and active microwave data.” IEEE International Geoscience and Remote Sensing Symposium.

Liu, W., Baret, F., Xingfa, G., Zhang, B., Tong, Q., and Zheng, L. (2010). “Evaluation of methods for soil surface moisture estimation from reflectance data.” International Journal of Remote Sensing, 24(10), 2069–2083 .

Liu, Z., Xu, Z., Fu, G., and Yao, Z. (2013). “Assessing the hydrological impacts of climate change in the headwater catchment of the Tarim River basin, China.” Hydrology Research, 44(5), 834.

Lu, S., Ren, T., Gong, Y., and Horton, R. (2007). “An Improved Model for Predicting Soil Thermal Conductivity from Water Content at Room Temperature.” Soil Science Society of America Journal, 71(1), 8.

Maltese, A., Bates, P., Capodici, F., Cannarozzo, M., Ciraolo, G., and Loggia, G. L. (2013). “Critical analysis of thermal inertia approaches for surface soil water content retrieval.” Hydrological Sciences Journal, 58(5), 1144–1161.

McVicar, T. R., Van Niel, T. G., Li, L., King, E. A., and Donohue, R. J. (2007). Deriving moisture availability from time series remote sensing for ecohydrological applications: Development of a prototype near real-time operational system. Deriving moisture availability from time series remote sensing for ecohydrological applications: Development of a prototype near real-time operational system, rep., CSIRO Land and Water Science Report 37/07, Canberra, AU.

Melesse, A. M. (2004). "Spatiotemporal dynamics of land surface parameters in the Red River of the North Basin." Physics and Chemistry of the Earth, Parts A/B/C, 29(11-12), 795–810.

Menenti, M. (1984). Physical aspects and determination of evaporation in deserts applying remote sensing techniques. EV, Wageningen.

Micasense (2015). Micasense RedEdge™ 3 Multispectral Camera User Manual. Micasense Inc., Seattle, WA.

Minacapilli, M., Iovino, M., and Blanda, F. (2009). "High resolution remote estimation of soil surface water content by a thermal inertia approach." Journal of Hydrology, 379(3-4), 229–238.

Monteith, J. L., and Unsworth, M. H. (2008). Principles of environmental physics. Elsevier/Acad. Press, Amsterdam.

Muller, E., and Décamps, H. (2001). "Modeling soil moisture–reflectance." Remote Sensing of Environment, 76(2), 173–180.

Murphy, J. A. (2002). "Best Management Practices for Irrigating Golf Course Turf." Best Management Practices for Irrigating Golf Course Turf, Rutgers Cooperative Extension, New Brunswick, NJ.

Nadler, A., Dasberg, S., and Lapid, I. (1991). "Time Domain Reflectometry Measurements of Water Content and Electrical Conductivity of Layered Soil Columns." Soil Science Society of America Journal, 55(4), 938.

NASA (2017a). “SMAP: Instrument.” (2017b). NASA, <https://smap.jpl.nasa.gov/observatory/instrument/> (May 8, 2017).

NASA (2017b). “Measuring Vegetation: NDVI and EVI.” (2017a). NASA, <https://earthobservatory.nasa.gov/Features/MeasuringVegetation/measuring_vegetation_2.php> (May 8, 2017).

Pierdicca, N., Pulvirenti, L., Santarelli, A., Crapolicchio, R., Talone, M., and Puca, S. (2012). “Comparison of microwave passive and active observations of soil moisture.” 2012 IEEE International Geoscience and Remote Sensing Symposium.

Pohn, H. A., Offield, T. W., and Watson, K. (1974). “Thermal inertia mapping from satellite discrimination of geologic units in Oman.” Journal of Research of U. S. Geological Survey, 2, 147–159.

Ponizovsky, A., Chudinova, S., and Pachepsky, Y. (1999). “Performance of TDR calibration models as affected by soil texture.” Journal of Hydrology, 218(1-2), 35–43.

Price, J. C. (1977). “Thermal inertia mapping: A new view of the Earth.” Journal of Geophysical Research, 82(18), 2582–2590.

Qin, Q., Ghulam, A., Zhu, L., Wang, L., Li, J., and Nan, P. (2008). “Evaluation of MODIS derived perpendicular drought index for estimation of surface dryness over northwestern China.” International Journal of Remote Sensing, 29(7), 1983–1995.

Quilter, M., and Anderson, V. (2006). “A proposed method for determining shrub utilization using (LA/LS) imagery.” Journal of Range Management, 54(4).

Rowlandson, Tracy L., Aaron A. Berg, Paul R. Bullock, E. Rotimi Ojo, Heather Mcnairn, Grant Wiseman, and Michael H. Cosh. "Evaluation of several calibration procedures for a portable soil moisture sensor." Journal of Hydrology 498 (2013): 335-44. doi:10.1016/j.jhydrol.2013.05.021.

Sabins, F. F. (2007). Remote sensing: principles and interpretation. Waveland Press, Long Grove, IL.

Santanello, J. A., and Friedl, M. A. (2003). "Diurnal Covariation in Soil Heat Flux and Net Radiation." Journal of Applied Meteorology, 42(6), 851–862.

Santi, E., Paloscia, S., Pettinato, S., Notarnicola, C., Pasolli, L., and Pistocchi, A. (2013). "Comparison between SAR Soil Moisture Estimates and Hydrological Model Simulations over the Scrivia Test Site." Remote Sensing, 5(10), 4961–4976.

Saxton, K. E., and Rawls, W. J. (2006). "Soil Water Characteristic Estimates by Texture and Organic Matter for Hydrologic Solutions." Soil Science Society of America Journal, 70(5), 1569.

Schmugge, T. J., Meneely, J. M., Rango, A., and Neff, R. (1977). "Satellite Microwave Observations of Soil Moisture Variations." Journal of the American Water Resources Association, 13(2), 265–282.

Schmugge, T., and Jackson, T. (1997). "Passive Microwave Remote Sensing of Soil Moisture." Land Surface Processes in Hydrology, 239–262.

Sellers, P. (1987). "Relations between canopy reflectance, photosynthesis and transpiration: Links between optics, biophysics and canopy architecture." Advances in Space Research, 7(11), 27–44.

Shintani, C., and Fonstad, M. A. (2017). "Comparing remote-sensing techniques collecting bathymetric data from a gravel-bed river." International Journal of Remote Sensing, 1–20.

Shuttleworth, W., Zreda, M., Zeng, X., Zweck, C., and Ferré, T. (2010). "The COsmic-ray Soil Moisture Observing System (COSMOS): a non-invasive, intermediate scale soil moisture measurement network." Role of hydrology in managing consequences of a changing global environment.

Singh, R. K., Irmak, A., Irmak, S., and Martin, D. L. (2008). “Application of SEBAL Model for Mapping Evapotranspiration and Estimating Surface Energy Fluxes in South-Central Nebraska.” Journal of Irrigation and Drainage Engineering, 134(3), 273–285.

Soliman, A., Heck, R., Brenning, A., Brown, R., and Miller, S. (2013). “Remote Sensing of Soil Moisture in Vineyards Using Airborne and Ground-Based Thermal Inertia Data.” Remote Sensing, 5(8), 3729–3748.

St. Hilaire, R., Arnold, M. A., Wilkerson, D. C., Devitt, D. A., Hurd, B. H., Lesikar, B. J., Lohr, V. I., Martin, C. A., McDonald, G. V., Morris, R. L., Pittenger, D. R., Shaw, D. A., and Zoldoske, D. F. (2008). “Efficient Water Use in Residential Urban Landscapes.” HortScience, 43(7), 2081–2092.

Swain, K. C. (2007). “Suitability of low-altitude remote sensing images for estimating nitrogen treatment variations in rice cropping for precision agriculture adoption.” Journal of Applied Remote Sensing, 1(1), 013547.

Swain, K. C., Thomson, S. J., and Jayasuriya, H. P. W. (2010). “Adoption of an Unmanned Helicopter for Low-Altitude Remote Sensing to Estimate Yield and Total Biomass of a Rice Crop.” Transactions of the ASABE, 53(1), 21–27.

Sun, Z., Gebremichael, M., Wang, Q., Wang, J., Sammis, T., and Nickless, A. (2013). “Evaluation of Clear-Sky Incoming Radiation Estimating Equations Typically Used in Remote Sensing Evapotranspiration Algorithms.” Remote Sensing, 5(10), 4735–4752.

Tamminga, A., Hugenholtz, C., Eaton, B., and Lapointe, M. (2014). “Hyperspatial Remote Sensing of Channel Reach Morphology and Hydraulic Fish Habitat Using an Unmanned Aerial Vehicle (UAV): A First Assessment in the Context of River Research and Management.” River Research and Applications, 31(3), 379–391.

Tarnawski, V. R., and Leong, W. H. (2000). “Thermal Conductivity of Soils at Very Low Moisture Content and Moderate Temperatures.” Transport in Porous Media, 41(2), 137–147.

TexasET Network. (2017). TexasET Network, <http://texaset.tamu.edu/> (Oct. 31, 2017).

Texas Water Development Board Water Use Survey. (2017). Texas Water Use Estimates: 2015 Summary. Austin, TX.

Tijerina, L., Coffey, J., Mcguire, M., Atkinson, E., and Gaughan, M. (2016). "Tarrant Regional Water District: Integrated Pipeline; Real-Time As-Built for Construction." Pipelines 2016.

Topp, G. C. (2003). "State of the art of measuring soil water content." Hydrological Processes, 17(14), 2993–2996.

Trenholm, L. E., Schlossberg, M. J., Lee, G., Parks, W., and Geer, S. A. (2000). "An evaluation of multi-spectral responses on selected turfgrass species." International Journal of Remote Sensing, 21(4), 709–721.

Turner, D., Lucieer, A., and Watson, C. (2012). "An Automated Technique for Generating Georectified Mosaics from Ultra-High Resolution Unmanned Aerial Vehicle (UAV) Imagery, Based on Structure from Motion (SfM) Point Clouds." Remote Sensing, 4(12), 1392–1410.

Ulaby, F. T., Moore, R. K., and Fung, A. K. (1990). Microwave remote sensing. Active and passive. Artech House, Norwood.

United Nations, Department of Economic and Social Affairs, Population Division (2014). World Urbanization Prospects: The 2014 Revision, Highlights." United Nations, New York, NY.

Valavanis, K. P., and Kontitsis, M. (2007). "A Historical Perspective on Unmanned Aerial Vehicles." Advances in Unmanned Aerial Vehicles Intelligent Systems, Control and Automation: Science and Engineering, 15–46.

Vereecken, H., Huisman, J., Pachepsky, Y., Montzka, C., Kruk, J. V. D., Bogena, H., Weihermüller, L., Herbst, M., Martinez, G., and Vanderborght, J. (2014). "On the spatio-temporal dynamics of soil moisture at the field scale." Journal of Hydrology, 516, 76–96.

Veroustraete, F., Li, Q., Verstraeten, W. W., Chen, X., Bao, A., Dong, Q., Liu, T., and Willems, P. (2011). “Soil moisture content retrieval based on apparent thermal inertia for Xinjiang province in China.” International Journal of Remote Sensing, 33(12), 3870–3885.

Verstraeten, W. W., Veroustraete, F., Sande, C. J. V. D., Grootaers, I., and Feyen, J. (2006). “Soil moisture retrieval using thermal inertia, determined with visible and thermal spaceborne data, validated for European forests.” Remote Sensing of Environment, 101(3), 299–314.

Wang, L., and Qu, J. J. (2009). “Satellite remote sensing applications for surface soil moisture monitoring: A review.” Frontiers of Earth Science in China, 3(2), 237–247.

Watson, K. (1971). “7th International Symposium on Remote Sensing of Environment.” 2017–2041.

Watson, K. (1982). “Regional thermal-inertia mapping from an experimental satellite.” Geophysics, 47(12), 1681–1687.

Wu, J., and Bauer, M. E. (2012). “Estimating Net Primary Production of Turfgrass in an Urban-Suburban Landscape with QuickBird Imagery.” Remote Sensing, 4(12), 849–866.

Xiang, H., and Tian, L. (2011). “Method for automatic georeferencing aerial remote sensing (RS) images from an unmanned aerial vehicle (UAV) platform.” Biosystems Engineering, 108(2), 104–113.

Xu, H. (2013). “Dynamic of soil exposure intensity and its effect on thermal environment change.” International Journal of Climatology, 34(3), 902–910.

Xue, Y., and Cracknell, A. P. (1995). “Advanced thermal inertia modelling.” International Journal of Remote Sensing, 16(3), 431–446.

Yang, S.-C., Shen, Y.-J., Guo, Y., and Kondoh, A. (2012). “Monitoring soil moisture by apparent thermal inertia method.” Chinese Journal of Eco-Agriculture, 19(5), 1157–1161.

Yu, X., Zhang, N., Pradhan, A., Thapa, B., and Tjuatja, S. (2015). “Design and Evaluation of a Thermo-TDR Probe for Geothermal Applications.” Geotechnical Testing Journal, 38(6), 20150023.

Zeng, Y., Feng, Z., and Xiang, N. (2004). “Assessment of soil moisture using Landsat ETM+ temperature/vegetation index in semiarid environment.” Proceedings of IGARSS 2004 IEEE International Geoscience and Remote Sensing Symposium.

Zhang, C., and Kovacs, J. M. (2012). “The application of small unmanned aerial systems for precision agriculture: a review.” Precision Agriculture, 13(6), 693–712.

Zhang, D., Tang, R., Zhao, W., Tang, B., Wu, H., Shao, K., and Li, Z.-L. (2014). “Surface Soil Water Content Estimation from Thermal Remote Sensing based on the Temporal Variation of Land Surface Temperature.” Remote Sensing, 6(4), 3170–3187.

Zhang, D., and Zhou, G. (2016). “Estimation of Soil Moisture from Optical and Thermal Remote Sensing: A Review.” Sensors, 16(8), 1308.

Zribi, M., Gorrab, A., Baghdadi, N., Lili-Chabaane, Z., and Mougenot, B. (2014). “Influence of Radar Frequency on the Relationship between Bare Surface Soil Moisture Vertical Profile and Radar Backscatter.” IEEE Geoscience and Remote Sensing Letters, 11(4), 848–852.

BIOGRAPHICAL INFORMATION

Kevin James Wienhold obtained a Bachelor of Science in Environmental Science with specialization in hydrology and hydraulics at Cleveland State University in 2014. Kevin's interest in remote sensing started in 2010 when he began performing aerial surveys as a volunteer pilot for the Nature Conservancy of Ohio. He started his Master program at the University of Texas at Arlington in spring 2015 under supervision of Dr. Nick Fang, who was among the first academic leaders in the DFW Metroplex to conduct unmanned aerial vehicle (UAV) missions for the acquisition of flood prediction data, water quality assessment and other water-related issues. Kevin continued to gain significant experience with GIS and remote sensing as well as stochastic hydrology and hydrologic and hydraulic modeling. In addition to his academic experience, Kevin worked for one year at GHD as an environmental technologist, performing groundwater remediation, sampling of various media, including water, air and soil, and providing contractor oversight for environmental health and safety.